

Striped Superconductor in Rhombohedral Hexalayer Graphene

Erin Morissette^{1,*}, Peiyu Qin^{1,*}, Hai-Tian Wu¹, Naiyuan J. Zhang¹,
Ron Q. Nguyen¹, K. Watanabe², T. Taniguchi³, and J.I.A. Li^{1,4†}

¹Department of Physics, Brown University, Providence, RI 02912, USA

²Research Center for Functional Materials, National Institute for Materials Science, 1-1 Namiki, Tsukuba 305-0044, Japan

³International Center for Materials Nanoarchitectonics,

National Institute for Materials Science, 1-1 Namiki, Tsukuba 305-0044, Japan and

⁴Department of Physics, University of Texas at Austin, Austin, TX 78712, USA

(Dated: August 11, 2025)

The nature of a superconductor is fundamentally determined by the symmetries broken in its order parameter. Here, we report an exceptionally exotic superconducting phase in rhombohedral hexalayer graphene that simultaneously breaks rotational, translational, and time-reversal symmetries. We show that superconductivity emerges from a quarter-metallic state and is accompanied by the onset of stripe charge order. This unique intertwinement is revealed by angle-resolved transport measurements, which demonstrate dissipationless current confined to a single principal axis—forming one-dimensional-like superconducting channels—while the orthogonal direction remains resistive down to the lowest temperatures. The formation of stripe order is marked by a first-order melting transition, evidenced by pronounced thermal hysteresis upon warming and cooling. In addition, magnetic-field-induced switching between superconducting states—reminiscent of behavior previously observed in rhombohedral tetra- and pentalayer graphene—signals time-reversal symmetry breaking. Collectively, these observations reveal a previously unrecognized quantum phase: a chiral superconductor embedded within a stripe-ordered anomalous Hall state.

The symmetries in a superconducting phase—or their absence—serve as powerful fingerprints for identifying the nature of the underlying order parameter. A classic example is the superfluid A-phase of ^3He , which emerges around 2 mK in the strong-coupling regime and simultaneously breaks rotational and time-reversal symmetries [1]. This unique combination arises from Cooper pairs carrying nonzero angular momentum, rendering the A-phase both a p -wave superconductor and an orbital ferromagnet [2–4]. In a different vein, experimental evidence from many cuprate superconductors points to the presence of a stripe phase, where superconductivity coexists with smectic electronic order—characterized by the simultaneous breaking of rotational and translational symmetries [5–7]. The stripe order establishes an important conceptual connection linking together an array of intertwined orders that have largely defined our under-

standing of superconductivity in cuprate materials.

More recently, rhombohedral multilayer graphene has emerged as an intriguing platform for exploring novel superconducting phases. Like other strongly correlated electron systems, the low-temperature phase diagrams of rhombohedral multilayer graphene host a rich spectrum of coexisting and competing orders [8–12]. Notably, in rhombohedral graphene with different layer numbers, superconducting phases are shown to exhibit unusual interplay with half and quarter metal phases [13–17]. In particular, the Cooper pairing instability in tetra- and pentalayer rhombohedral graphene (R4G and R5G) occurs from a quarter metal normal phase that displays the anomalous Hall effect [16, 18–23]. The resulting superconducting phase exhibits magnetic-field-driven switching between distinct ground states—closely resembling the hallmark behavior of the ^3He A-phase [16].

Here, we expand on prior observations in rhombohedral multilayer graphene and report a previously unrecognized superconducting phase in rhombohedral hexalayer graphene (R6G), which unifies the defining characteristics of both the ^3He A-phase and striped superconductors. In R6G, the superconducting state emerges with simultaneous breaking of rotational, translational, and time-reversal symmetries. This unprecedented combination of broken symmetries defines a novel order parameter structure, revealing a new frontier in the study of unconventional superconductivity.

To identify the striped superconductor, we leverage recent advances in angle-resolved transport techniques [24–30], which offer powerful tools for probing how intertwined electronic orders emerge and evolve alongside superconductivity. The R6G sample is assembled into a heterostructure consisting of dual encapsulation of hexagonal boron nitride and graphite, as illustrated in Fig. 1a [31–33]. This heterostructure is further patterned into a disk geometry, with $2.5\ \mu\text{m}$ in diameter and eight evenly spaced electrical leads (Fig. 1b) [27–30]. The dual-gated geometry allows independent control of carrier density n and displacement field D , defining a two-dimensional phase space.

In angle-resolved measurements, the angle ϕ is defined by the orientation of the source (S) and drain (D) contacts. For each value of ϕ , the parallel and transverse re-

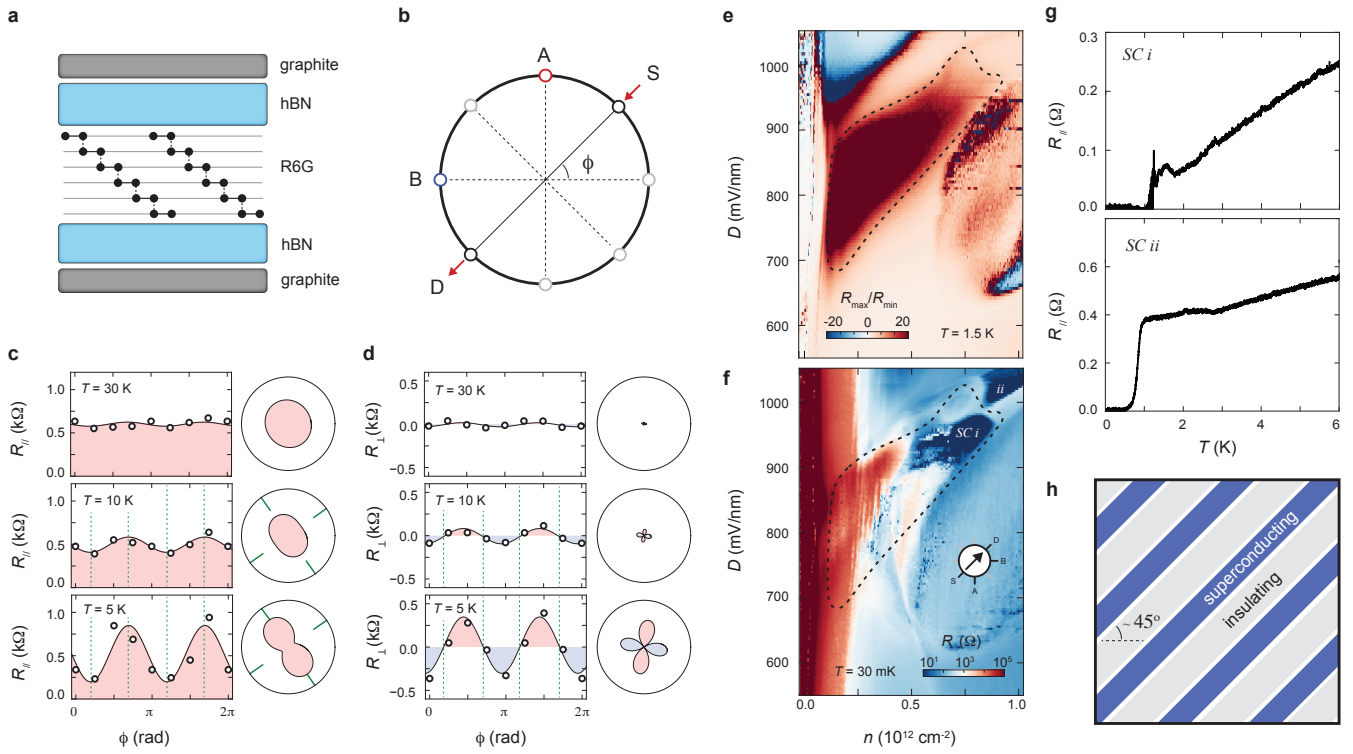


FIG. 1. **Transport anisotropy and superconductivity in rhombohedral hexalayer graphene.** (a) Schematic diagram of the R6G heterostructure. (b) Sunflower sample geometry with a disk-shaped channel and eight evenly spaced leads. (c–d) Angle-resolved measurements of (c) R_{\parallel} and (d) R_{\perp} above the superconducting transition temperature at $T = 30$ K (top), 10 K (middle), and 5 K (bottom). Solid curves denote best fits using Eqs. (M1) and (M2). The angular oscillations indicate two principal axes aligned along $\phi = 45^\circ$ and 135° . (e) Color-scale map of transport anisotropy at $T = 1.5$ K, characterized by the resistance ratio between measurements along orthogonal principal axes. Black dashed lines encircle regions of strong anisotropy, where $R_{\max}/R_{\min} > 5$. (f) Color-scale map of the longitudinal resistance R_{\parallel} , measured at $T = 40$ mK, $B = 0$, along $\phi = 45^\circ$, as a function of carrier density n and displacement field D . Inset: measurement configuration. (g) R – T curves measured from superconducting regions $SC\ i$ and $SC\ ii$. (h) Schematic diagram illustrating the coexistence of stripe order and superconductivity.

sistances, R_{\parallel} and R_{\perp} , are extracted from the measured voltage responses between different contact pairs. Figures 1c–d display the angular dependence of R_{\parallel} and R_{\perp} at various temperatures in the large displacement field (D) limit. The solid black curves show the best fits to the expected angular form (Eq. M1 and M2) [24, 26]. At $T = 30$ K, the transport is nearly isotropic. However, as the temperature is lowered, a pronounced anisotropy emerges near $T = 10$ K, manifested by the clear angular oscillations in both R_{\parallel} and R_{\perp} . The principal axes of this transport anisotropy—corresponding to the directions of maximum and minimum resistance—are aligned along $\phi = 45^\circ$ and 135° , respectively.

For the remainder of this work, we focus on exploring the regime of the stripe order, encircled by the black dashed line in Fig. 1e. At $T = 1.5$ K, which is above the superconducting transition temperature, the normal state in this region exhibits pronounced transport anisotropy, evidenced by the large resistance ratio between orthogonal principal axes, highlighted in red and white in the n – D map. Upon further cooling, two su-

perconducting pockets emerge near the boundary of the stripe order, reflected by vanishing R_{\parallel} measured along the principal axis of maximum conductivity, shown as dark blue in Fig. 1f. For simplicity, these superconducting regimes are labeled $SC\ i$ and $SC\ ii$. Their superconducting transitions are evident in the R – T characteristics displayed in Fig. 1g, showing sharply defined transition around $T = 1$ K for both superconducting phases.

In the following, we show that electrons form metallic and insulating stripes oriented along $\phi = 45^\circ$ in the stripe regime. The $SC\ i$ phase coexists with the stripe order, forming one-dimensional superconducting channels, which can be identified based on the characteristic angular dependence in the transport response.

First, we examine the nature of transport anisotropy measured within the $SC\ i$ pocket above the superconducting transition, which is quantified by defining an anisotropy parameter as

$$\xi = \frac{R_{\max} - R_{\min}}{R_{\max} + R_{\min}}. \quad (1)$$

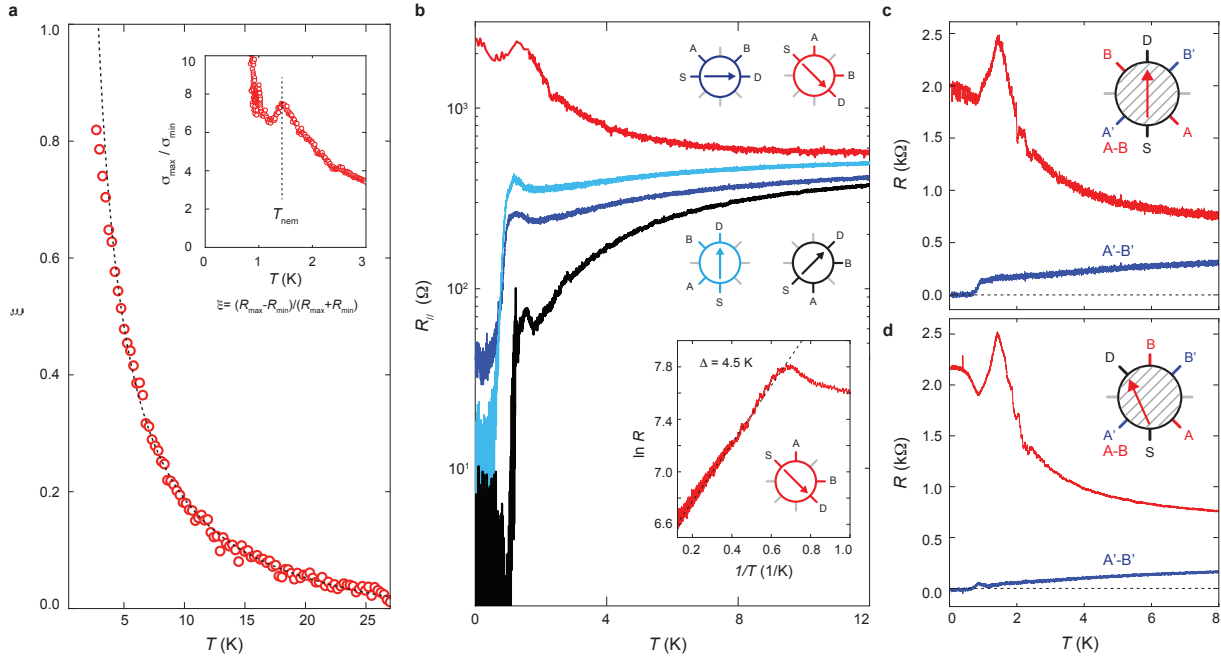


FIG. 2. Extreme anisotropy in superconducting transport. (a) Temperature dependence of the transport anisotropy, defined in Eq. 1, which follows a Curie–Weiss behavior (black dashed line). Inset: Conductivity ratio between orthogonal principal axes exhibits a cusp around $T = 1.4$ K, indicating the nematic transition temperature T_{nem} . (b) Temperature dependence of R_{\parallel} measured with current flowing along different directions. Inset: Arrhenius plot of the R – T curve measured along $\phi = 135^\circ$, revealing a thermally activated gap $\Delta \approx 4.5$ K. (c–d) R – T traces measured in alternative configurations distinct from R_{\parallel} . The observation of superconducting or insulating responses is solely determined by the alignment of voltage probes relative to the stripe orientation. All measurements are performed at $n = 0.74 \times 10^{12} \text{ cm}^{-2}$ and $D = 958 \text{ mV/nm}$, within the SC i region.

Here, the maximum and minimum resistance values, R_{\max} and R_{\min} , are obtained when current is applied along the principal axes of the transport anisotropy. As such, ξ characterizes the contrast between the orthogonal principal directions (see also Eq. M1–M2) [26, 29, 30]. Figure 2a shows the temperature dependence of ξ , which exhibits excellent agreement with the Curie–Weiss law.

The inset of Fig. 2a plots the intrinsic anisotropy ratio $\sigma_{\max}/\sigma_{\min}$, extracted from the angular dependence of R_{\parallel} and R_{\perp} (Fig. 1c–d) using the theoretical framework developed in Refs. [26, 27]. Most notably, $\sigma_{\max}/\sigma_{\min}$ displays a pronounced cusp near $T = 1.4$ K. Taken together with the Curie–Weiss behavior at higher temperatures, these results point to a nematic instability occurring immediately above the superconducting transition [34–36].

Upon further lowering the temperature, the emergence of superconductivity reveals a highly unusual angular dependence in transport. Figure 2b shows R_{\parallel} as a function of temperature measured at various angles ϕ . When current is applied along the principal axis of maximum conductivity (i.e., minimum resistivity, at $\phi = 45^\circ$), a sharply defined superconducting transition appears at $T_c = 1.1$ K, evidenced by the vanishing of R_{\parallel} (black trace in Fig. 2b). In contrast, a markedly different response occurs when current flows along the orthogonal direc-

tion ($\phi = 135^\circ$). As shown by the red trace in Fig. 2b, transport remains highly resistive down to the base temperature of the dilution refrigerator ($T = 30$ mK), with no indication of superconductivity.

Notably, along the principal axis of minimum conductivity, R_{\parallel} exhibits thermally activated insulating behavior, as shown in the inset of Fig. 2b. A linear fit to the Arrhenius plot yields an energy gap of approximately $\Delta \approx 4.5$ K, in stark contrast to the metallic response observed along the orthogonal direction. The emergence of activated insulating behavior along only one principal axis is unprecedented, which points to the formation of an exotic electronic order that extends beyond a fluid-like nematic phase.

The extreme anisotropy observed in our transport measurements is reminiscent of the quantum Hall stripe phases [37–40], yet it is distinguished by the absence of Landau level formation and by the emergence of superconductivity away from the resistive axis. We propose that these observations point to a coexistence between superconductivity and a stripe charge order, or an electronic smectic phase [37–42], with the easy axis aligned along the direction of maximum conductivity at $\phi = 45^\circ$.

Crucially, the angular interplay between superconductivity and stripe order does not depend on the specific

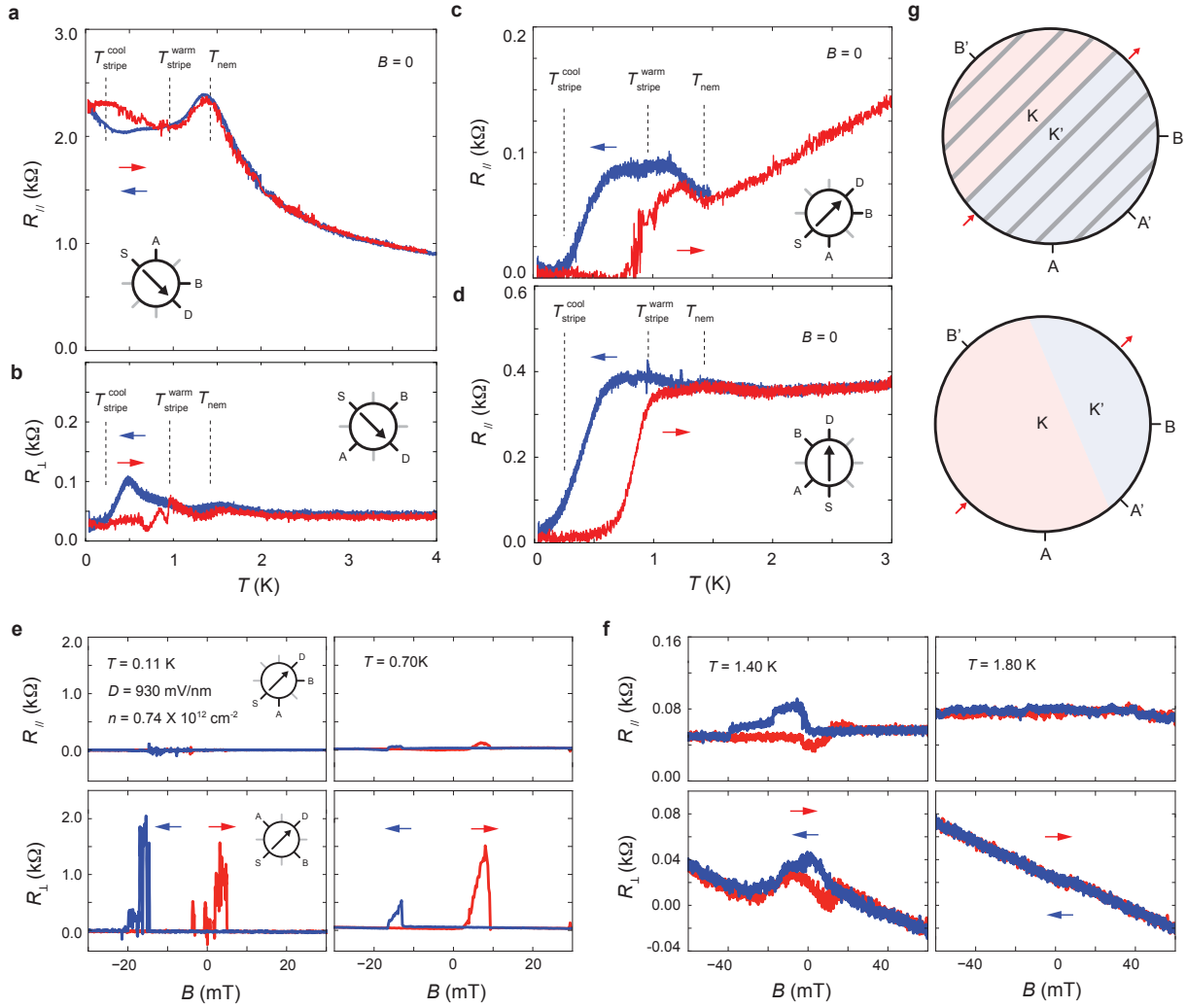


FIG. 3. Temperature- and magnetic-field-driven hysteretic transitions. (a–b) Temperature sweeps of (a) R_{\parallel} and (b) R_{\perp} , measured during both warming and cooling cycles with current applied perpendicular to the stripe orientation at $\phi = 135^\circ$. (c–d) R_{\parallel} versus T measured during both warming and cooling cycles along (c) $\phi = 225^\circ$ and (d) $\phi = 270^\circ$, showing prominent hysteresis in the superconducting transition. Measurements are performed at $D = 954$ mV/nm and $n = 0.74 \times 10^{12} \text{ cm}^{-2}$. (e–f) R_{\parallel} (top) and R_{\perp} (bottom), measured as the out-of-plane magnetic field B is swept back and forth, with current flowing parallel to the stripe direction at $\phi = 45^\circ$. Data in (e) and (f) are taken below and above the superconducting transition temperature, respectively. All measurements are performed at $D = 930$ mV/nm and $n = 0.74 \times 10^{12} \text{ cm}^{-2}$. (g) Schematic illustration: in the stripe phase, domain boundaries between valley K and K' align with the stripe orientation, generating resistive responses in R_{\perp} but not R_{\parallel} . Above the melting transition, these domain boundaries are no longer locked to a principal axis, leading to hysteresis in both R_{\perp} and R_{\parallel} .

measurement configuration. Instead, we find that the superconducting or insulating response is determined solely by the alignment of the voltage probes relative to the stripe orientation. Figures 2c and d illustrate two such examples, where alternative configurations—with different current flow directions and voltage measurement geometries, distinct from R_{\parallel} and R_{\perp} —are employed. In both setups, voltage probes positioned perpendicular to the stripe direction (A, B) display an insulating response, while probes aligned along the stripe direction (A', B') exhibit a vanishing resistance as the temperature is low-

ered (see Fig. M10 and Fig. M11 for measurements performed with additional configurations). These observations confirm that the unique angular dependence arises from an intrinsic coexistence of superconductivity and stripe order, rather than from artifacts related to specific measurement configurations.

A key distinction between smectic and nematic phases is the presence of crystalline order associated with translational symmetry breaking. As further support for the existence of such crystalline order, we observe a clear first-order melting transition, characterized by pro-

nounced supercooling and superheating. This transition manifests as hysteresis in the temperature dependence of the insulating response. When current is applied perpendicular to the stripe direction at $\phi = 135^\circ$, both R_{\parallel} and R_{\perp} exhibit hysteretic behaviors between controlled warming and cooling cycles (Figs. 3a–b; see also SI for details [43]). Notably, the transport responses differ significantly between warming and cooling; for example, a resistance peak in R_{\perp} appears only during the cooling cycle. These features provide compelling evidence for an intrinsic first-order transition and effectively rule out experimental artifacts.

Interestingly, the hysteresis in the $R-T$ curves emerges at a temperature lower than the resistive cusp previously identified as the nematic transition (Fig. 3a). This suggests that two distinct transitions take place sequentially upon cooling: first, a nematic transition marks the onset of an anisotropic fluid phase at T_{nem} , indicated by the cusp in R_{\parallel} ; and second, a smectic transition indicates the formation of stripe order at T_{stripe} , defined by the thermal hysteresis. Due to the first-order nature of this smectic transition, we mark the stripe formation temperature on warming and cooling as $T_{\text{stripe}}^{\text{warm}}$ and $T_{\text{stripe}}^{\text{cool}}$, respectively (Figs. 3a–b).

Most remarkably, the emergence of superconductivity appears in lock step with the stripe formation on both warming and cooling. As illustrated in Figs. 3c–d, the superconducting transition—defined by the vanishing of R_{\parallel} —occurs around the same temperature as stripe formation on both cooling and warming. As a result, the superconducting transition temperature is significantly lower during cooling compared to warming, indicative of a first-order transition.

The presence of hysteresis in the superconducting transition is highly unusual and typically occurs between superconducting phases with distinct order parameters, such as the A- and B-phases of superfluid ^3He [1]. For the $SC\ i$ phase in R6G, this hysteresis may naturally arise from the supercooling and superheating associated with the melting of the coexisting stripe order. The tight coupling between stripe formation and the onset of superconductivity further supports the picture illustrated in Fig. 1h, where superconducting channels emerge between insulating stripes.

For completeness, we note that more exotic scenarios cannot be entirely ruled out. One such possibility is a temperature-driven transition between two distinct superconducting phases, analogous to the A- and B-phases of superfluid ^3He . In this case, the observed hysteresis would result from supercooling and superheating across a first-order phase boundary [44–46].

Beyond its coexistence with stripe order, the $SC\ i$ phase also exhibits clear signatures of broken time-reversal symmetry, as evidenced by hysteretic transitions in the superconducting phase driven by an out-of-plane magnetic field (B_{\perp}). Figure 3e shows transport responses

measured with current flowing along the stripe direction at $T < T_c$, while B_{\perp} is swept back and forth. Field-induced transitions appear as prominent peaks in R_{\perp} , while both R_{\parallel} and R_{\perp} remain vanishingly small away from these transitions.

This behavior is consistent with recent observations in rhombohedral tetra- and pentalayer graphene [16], where similar hysteresis has been interpreted as a signature of chiral superconductivity. Indeed, a B -induced first-order transition in a superconductor is closely analogous to the A-phase of superfluid ^3He —a paradigm example of a chiral superconductor [4]. An out-of-plane magnetic field reverses the angular momentum of the p -wave superconductor, resulting in hysteretic switching between degenerate chiral configurations.

In R6G, the magnetic-field–driven hysteresis persists to above the superconducting transition temperature. At $T = 1.4$ K (Fig. 3f), the hysteretic behavior indicates an anomalous Hall effect arising from topological orbital magnetism [47–49]. This suggests that superconductivity in R6G arises from a valley polarized normal state. Intriguingly, the onset of the anomalous Hall effect coincides with the nematic transition at T_{nem} , pointing to a direct link between rotational and time-reversal symmetry breaking. This is reminiscent of a previous observation in R6G, showing that the emergence of the anomalous Hall effect coincides with the nematic transition near zero displacement field ($D \approx 0$) [29]. Taken together, these observations suggest that time-reversal and rotational symmetry breaking in R6G, and potentially other rhombohedral multilayer structures, share a common origin. A possible mechanism could be spontaneous momentum space condensation, which has been proposed to occur in near the flat band edge of multilayer graphene heterostructures [18, 50–53].

We note that the resistive response of the magnetic-field–driven transition exhibits a unique angular dependence below the stripe formation temperature. As shown in Fig. 3e, the field-driven transition is marked by a pronounced peaks in R_{\perp} . However, R_{\parallel} remains largely featureless across the same transitions.

This angular dependence can be understood by considering the boundary between K and K' domains. In a superconducting phase, resistive response occurs when a domain boundary separates two voltage probes. In this scenario, a resistive response reflects the potential drop across the domain boundary. As such, the unique angular dependence in Fig. 3e indicates a tendency for domain boundaries between opposite valley to align along the stripe order, as illustrated in Fig. 3g. In this configuration, a potential drop across the domain wall is always detectable between A' and B' , whereas it is mostly absent between A and B .

This interpretation is further supported by the behavior of the field-driven transition above the stripe melting temperature. In this regime, a single hysteresis loop ap-

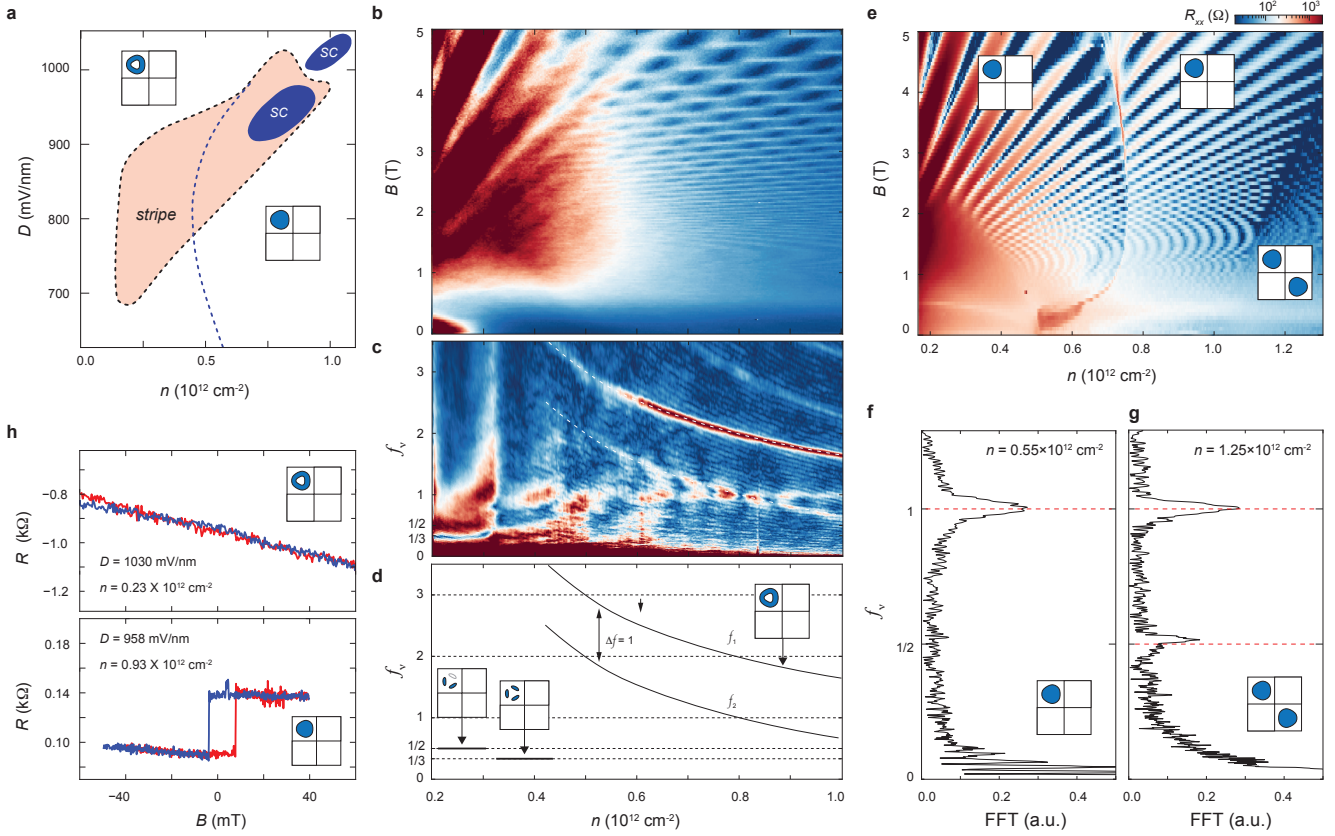


FIG. 4. **Fermiology, quarter- and half-metal states.** (a) Schematic n - D map showing the stripe regime as the shaded red area. (b) R_{\parallel} as a function of n and B , measured in the upper-left corner of the n - D map at $D = 1065$ mV/nm. (c) Fourier transform of quantum oscillations in (b). (d) Solid lines indicate the center frequencies of the most prominent peaks in f_v from (c). Inset: illustration of possible Fermi surface contours across different density regimes, including an annular Fermi sea on the low-density side of the stripe regime. (e) R_{\parallel} as a function of n and B , measured in the lower-right corner of the n - D map at $D = 650$ mV/nm. (f-g) Fourier spectrum amplitudes of data from (e), highlighting the quarter-metal state at $n = 0.55 \times 10^{12} \text{ cm}^{-2}$ in (f), and the half-metal state at $n = 1.25 \times 10^{12} \text{ cm}^{-2}$ in (g). (h) Resistance as a function of magnetic field swept back and forth, exhibiting hysteresis on the high-density side of the stripe regime, but no hysteresis on the low-density side.

pears in both R_{\parallel} and R_{\perp} (left panel of Fig. 3f), consistent with a domain wall misaligned relative to the voltage probes, as illustrated schematically in Fig. 3h. Notably, field-driven transitions similar to those shown in Fig. 3e persist even when superconductivity is suppressed by a large D.C. current bias (see Fig. M6). This observation suggests that the distinctive transport features in Fig. 3e originate primarily from the interplay between valley domains and stripe order, rather than from the superconducting phase itself.

Lastly, we investigate the fermiology of the stripe order by analyzing the Shubnikov–de Haas (SdH) quantum oscillations. Figure 4a shows a schematic diagram of the n - D phase space around the stripe regime, which is highlighted as a red shaded area. SdH oscillations are notably absent in the stripe regime. This could be a direct consequence of stripe formation, which substantially distorts the Fermi surface and suppresses SdH oscillation. Therefore, we focus on analyzing the portions of the phase

space that surround the stripe regime.

Figure 4b presents Shubnikov–de Haas (SdH) oscillations measured in the upper-left region of the n - D map, corresponding to the regime with lower carrier density and higher displacement field from the stripe order. The observed fish-net pattern reflects the coexistence of Fermi surfaces with electron- and hole-type carriers. A Fourier analysis reveals two dominant frequencies, f_1 and f_2 , satisfying $f_1 - f_2 = 1$ over a wide density range (Fig. 4c-d). We attribute this SdH oscillation to an annular-shaped Fermi sea, where a larger electron pocket coexists with a smaller hole pocket. Notably, the anomalous Hall effect is absent in this regime (top panel of Fig. 4h). This places an experimental constraint on the Berry curvature distribution across the annular-shaped Fermi sea.

On the high-density side of the stripe regime, the system enters a quarter-metal phase. Here, SdH oscillations display a dominant peak at $f_v = 1$ (Fig. 4f), consistent with a fully spin- and valley-polarized Fermi sea. This in-

terpretation is supported by the magnetic-field-induced hysteresis observed in transport measurements (bottom panel, Fig. 4h), confirming the presence of a quarter-metal phase. While the stripe order appears in between regimes of distinct Fermi sea topology, the observation of B_{\perp} -induced hysteresis points to a direct link with the quarter metal. A main distinction between the stripe order and the quarter-metal is the strength of anisotropy. The quarter-metal regime is mostly isotropic under angle-resolved transport measurement (see Fig. M5), whereas the stripe regime exhibits an extreme anisotropy ratio between orthogonal principal axes. At even higher carrier densities, the quarter metal evolves into a half-metallic state. This is indicated by a peak at $f_{\nu} = 1/2$ in the Fourier spectrum (Fig. 4e and g).

Taken together, our observations reveal a remarkable coexistence between multiple emergent orders. At a higher temperature of around $T = 1.5$ K, the onset of valley polarization is accompanied by a nematic transition. This gives rise to an anisotropic quarter-metal state, which likely originates from spontaneous momentum-space condensation [29].

As temperature is lowered, superconductivity and the stripe order emerge simultaneously from this anisotropic quarter metal. This simultaneous onset naturally leads to a spatial modulation of the superconducting gap, unlocking a promising platform for exploring pair density wave in 2D superconductors [54]. The magnetic-field-driven hysteresis in the superconducting phase reflects the chiral signature in the underlying order parameter [16]. Furthermore, the coexistence with the anomalous Hall effect points to a unique stripe order with two-fold rotation symmetry breaking [55–60].

It is worth noting that the superconducting transition temperature (T_c) in rhombohedral hexalayer graphene is significantly higher than in previously reported rhombohedral multilayer systems [14–16]. The observed increase in T_c , despite the coexistence with stripe charge order, raises new opportunities to explore exotic superconductivity characterized by nontrivial topology and multiple broken symmetries—an avenue certain to attract widespread future interest.

ACKNOWLEDGMENTS

J.I.A.L. wishes to thank Oskar Vafek for continued support and theoretical guidance in developing the novel scheme of angle-resolved transport measurement. J.I.A.L. also acknowledges helpful discussions with Sankar Das Sarma, Dima Feldman, Aaron Hui, Matthias Scheurer, Chunli Huang, and Boris Shklovskii. E.M. and J.I.A.L. acknowledge support from U.S. National Science Foundation under Award DMR-2143384. N.J.Z., and R.Q.N. acknowledge support from the Air Force Office of Scientific Research. K.W. and T.T. acknowl-

edge support from the JSPS KAKENHI (Grant Numbers 21H05233 and 23H02052) and World Premier International Research Center Initiative (WPI), MEXT, Japan. Part of this work was enabled by the use of pyscan (github.com/sandialabs/pyscan), scientific measurement software made available by the Center for Integrated Nanotechnologies, an Office of Science User Facility operated for the U.S. Department of Energy.

* These authors contributed equally to this work.

† jia.li@austin.utexas.edu

- [1] D. Vollhardt and P. Wölfle, *The Superfluid Phases of Helium 3* (Taylor and Francis, 1990).
- [2] V Ambegaokar, PG DeGennes, and D Rainer, “Landau-ginsburg equations for an anisotropic superfluid,” *Physical Review A* **9**, 2676 (1974).
- [3] P. M. Walsmley and A. I. Golov, “Chirality of superfluid $^3\text{He-}a$,” *Phys. Rev. Lett.* **109**, 215301 (2012).
- [4] H Ikegami, Y Tsutsumi, and K Kono, “Chiral symmetry breaking in superfluid $^3\text{He-}a$,” *Science* **341**, 59–62 (2013).
- [5] Erez Berg, Eduardo Fradkin, and Steven A Kivelson, “Theory of the striped superconductor,” *Physical Review B—Condensed Matter and Materials Physics* **79**, 064515 (2009).
- [6] Eduardo Fradkin, Steven A Kivelson, Michael J Lawler, James P Eisenstein, and Andrew P Mackenzie, “Nematic fermi fluids in condensed matter physics,” *The Annual Review of Condensed Matter Physics* **1**, 153–78 (2010).
- [7] Erez Berg, Eduardo Fradkin, and Steven A. Kivelson, “Charge-4e superconductivity from pair-density-wave order in certain high-temperature superconductors,” *Nature Physics* **5**, 830–833 (2009).
- [8] Eduardo Fradkin, Steven A. Kivelson, and John M. Tranquada, “Colloquium: Theory of intertwined orders in high temperature superconductors,” *Rev. Mod. Phys.* **87**, 457–482 (2015).
- [9] B Keimer and JE Moore, “The physics of quantum materials,” *Nature Physics* **13**, 1045–1055 (2017).
- [10] Rafael M Fernandes, Peter P Orth, and Jörg Schmalian, “Intertwined vestigial order in quantum materials: Nematicity and beyond,” *Annual Review of Condensed Matter Physics* **10**, 133–154 (2019).
- [11] Kevin P Nuckolls and Ali Yazdani, “A microscopic perspective on moiré materials,” *Nature Reviews Materials* **9**, 460–480 (2024).
- [12] Yaojia Wang, Heng Wu, Gregory T McCandless, Julia Y Chan, and Mazhar N Ali, “Quantum states and intertwining phases in kagome materials,” *Nature Reviews Physics* **5**, 635–658 (2023).
- [13] Haoxin Zhou, Tian Xie, Areg Ghazaryan, Tobias Holder, James R Ehrets, Eric M Spanton, Takashi Taniguchi, Kenji Watanabe, Erez Berg, Maksym Serbyn, *et al.*, “Half-and quarter-metals in rhombohedral trilayer graphene,” *Nature* **598**, 429–433 (2021).
- [14] Haoxin Zhou, Tian Xie, Takashi Taniguchi, Kenji Watanabe, and Andrea F Young, “Superconductivity in rhombohedral trilayer graphene,” *Nature* **598**, 434–438 (2021).
- [15] Haoxin Zhou, Ludwig Holleis, Yu Saito, Liam Cohen, William Huynh, Caitlin L Patterson, Fangyuan Yang,

Takashi Taniguchi, Kenji Watanabe, and Andrea F Young, “Isospin magnetism and spin-polarized superconductivity in bernal bilayer graphene,” *Science* **375**, 774–778 (2022).

[16] Tonghang Han, Zhengguang Lu, Zach Hadjri, Lihan Shi, Zhenghan Wu, Wei Xu, Yuxuan Yao, Armel A Cotten, Omid Sharifi Sedeh, Henok Weldeyesus, *et al.*, “Signatures of chiral superconductivity in rhombohedral graphene,” arXiv preprint arXiv:2408.15233 (2024).

[17] Youngjoon Choi, Ysun Choi, Marco Valentini, Caitlin L Patterson, Ludwig FW Holleis, Owen I Sheekey, Hari Stoyanov, Xiang Cheng, Takashi Taniguchi, Kenji Watanabe, *et al.*, “Superconductivity and quantized anomalous hall effect in rhombohedral graphene,” *Nature* **1**–6 (2025).

[18] Guillermo Parra-Martinez, Alejandro Jimeno-Pozo, Vo Tien Phong, Hector Sainz-Cruz, Daniel Kaplan, Peleg Emanuel, Yuval Oreg, Pierre A Pantaleon, Jose Angel Silva-Guillen, and Francisco Guinea, “Band renormalization, quarter metals, and chiral superconductivity in rhombohedral tetralayer graphene,” arXiv preprint arXiv:2502.19474 (2025).

[19] Yinqi Chen and Constantin Schrade, “Intrinsic superconducting diode effect and nonreciprocal superconductivity in rhombohedral graphene multilayers,” arXiv preprint arXiv:2503.16391 (2025).

[20] Yang-Zhi Chou, Jihang Zhu, and Sankar Das Sarma, “Intravalley spin-polarized superconductivity in rhombohedral tetralayer graphene,” arXiv preprint arXiv:2409.06701 (2024).

[21] Hui Yang and Ya-Hui Zhang, “Topological incommensurate fulde-ferrell-larkin-ovchinnikov superconductor and bogoliubov fermi surface in rhombohedral tetra-layer graphene,” arXiv preprint arXiv:2411.02503 (2024).

[22] Maine Christos, Pietro M Bonetti, and Mathias S Scheurer, “Finite-momentum pairing and superlattice superconductivity in valley-imbalanced rhombohedral graphene,” arXiv preprint arXiv:2503.15471 (2025).

[23] Chiho Yoon, Tianyi Xu, Yafis Barlas, and Fan Zhang, “Quarter metal superconductivity,” arXiv preprint arXiv:2502.17555 (2025).

[24] J Wu, AT Bollinger, X He, and I Božović, “Spontaneous breaking of rotational symmetry in copper oxide superconductors,” *Nature* **547**, 432–435 (2017).

[25] Jie Wu, Hari P Nair, Anthony T Bollinger, Xi He, Ian Robinson, Nathaniel J Schreiber, Kyle M Shen, Darrell G Schlom, and Ivan Božović, “Electronic nematicity in sr_2ruo_4 ,” *Proceedings of the National Academy of Sciences* **117**, 10654–10659 (2020).

[26] Oskar Vafek, “Anisotropic resistivity tensor from disk geometry magnetoconductance,” *Phys. Rev. Appl.* **20**, 064008 (2023).

[27] Dmitry V Chichinadze, Naiyuan James Zhang, Jiang-Xiazi Lin, Xiaoyu Wang, Kenji Watanabe, Takashi Taniguchi, Oskar Vafek, and JIA Li, “Observation of giant nonlinear hall conductivity in bernal bilayer graphene,” arXiv preprint arXiv:2411.11156 (2024).

[28] Naiyuan James Zhang, Jiang-Xiazi Lin, Dmitry V. Chichinadze, Yibang Wang, Kenji Watanabe, Takashi Taniguchi, Liang Fu, and J. I. A. Li, “Angle-resolved transport non-reciprocity and spontaneous symmetry breaking in twisted trilayer graphene,” *Nature Materials* **23**, 356–362 (2024).

[29] Erin Morissette, Peiyu Qin, K Watanabe, T Taniguchi, and JIA Li, “Intertwined nematicity, multiferroicity, and nonlinear hall effect in rhombohedral pentalayer graphene,” arXiv preprint arXiv:2503.09954 (2025).

[30] Naiyuan J Zhang, Pavel A Nosov, Ophelia Evelyn Sommer, Yibang Wang, Kenji Watanabe, Takashi Taniguchi, Eslam Khalaf, and JIA Li, “Angular interplay of nematicity, superconductivity, and strange metallicity in a moiré flat band,” arXiv preprint arXiv:2503.15767 (2025).

[31] A A Zibrov, C R Kometter, H Zhou, E M Spanton, T Taniguchi, K Watanabe, M P Zaletel, and A F Young, “Tunable interacting composite fermion phases in a half-filled bilayer-graphene landau level,” *Nature* **549**, 360–364 (2017).

[32] J. I. A. Li, C. Tan, S. Chen, Y. Zeng, T. Taniguchi, K. Watanabe, J. Hone, and C. R. Dean, “Even-denominator fractional quantum hall states in bilayer graphene,” *Science* **358**, 648–652 (2017).

[33] L Wang, I Meric, PY Huang, Q Gao, Y Gao, H Tran, T Taniguchi, K Watanabe, LM Campos, DA Muller, J Guo, P Kim, J Hone, K L Shepard, and C R Dean, “One-dimensional electrical contact to a two-dimensional material,” *Science* **342**, 614–617 (2013).

[34] Jiun-Haw Chu, Hsueh-Hui Kuo, James G Analytis, and Ian R Fisher, “Divergent nematic susceptibility in an iron arsenide superconductor,” *Science* **337**, 710–712 (2012).

[35] RM Fernandes, AV Chubukov, and J Schmalian, “What drives nematic order in iron-based superconductors?” *Nature physics* **10**, 97–104 (2014).

[36] Anna E Böhmer, Jiun-Haw Chu, Samuel Lederer, and Ming Yi, “Nematicity and nematic fluctuations in iron-based superconductors,” *Nature Physics* **18**, 1412–1419 (2022).

[37] MP Lilly, KB Cooper, JP Eisenstein, LN Pfeiffer, and KW West, “Evidence for an anisotropic state of two-dimensional electrons in high landau levels,” *Physical Review Letters* **82**, 394 (1999).

[38] M. P. Lilly, K. B. Cooper, J. P. Eisenstein, L. N. Pfeiffer, and K. W. West, “Anisotropic states of two-dimensional electron systems in high landau levels: Effect of an in-plane magnetic field,” *Phys. Rev. Lett.* **83**, 824–827 (1999).

[39] RR Du, DC Tsui, HL Stormer, LN Pfeiffer, KW Baldwin, and KW West, “Strongly anisotropic transport in higher two-dimensional landau levels,” *Solid State Communications* **109**, 389–394 (1999).

[40] W. Pan, R. R. Du, H. L. Stormer, D. C. Tsui, L. N. Pfeiffer, K. W. Baldwin, and K. W. West, “Strongly anisotropic electronic transport at landau level filling factor $\nu = 9/2$ and $\nu = 5/2$ under a tilted magnetic field,” *Phys. Rev. Lett.* **83**, 820–823 (1999).

[41] M. M. Fogler, A. A. Koulakov, and B. I. Shklovskii, “Ground state of a two-dimensional electron liquid in a weak magnetic field,” *Phys. Rev. B* **54**, 1853–1871 (1996).

[42] A. A. Koulakov, M. M. Fogler, and B. I. Shklovskii, “Charge density wave in two-dimensional electron liquid in weak magnetic field,” *Phys. Rev. Lett.* **76**, 499–502 (1996).

[43] Please see the supplementary materials.

[44] P Schiffer, MT O’keefe, MD Hildreth, Hiroshi Fukuyama, and DD Osheroff, “Strong supercooling and stimulation of the a-b transition in superfluid he 3,” *Physical review letters* **69**, 120 (1992).

[45] P Schiffer and DD Osheroff, “Nucleation of the ab transition in superfluid he 3: surface effects and baked alaska,” *Reviews of Modern Physics* **67**, 491 (1995).

[46] Yefan Tian, Dmytro Lotnyk, Anna Eyal, Kuang Zhang, Nikolay Zhelev, TS Abhilash, Aldo Chavez, EN Smith, Mark Hindmarsh, John Saunders, *et al.*, “Supercooling of the a phase of 3he,” *Nature communications* **14**, 148 (2023).

[47] Aaron L Sharpe, Eli J Fox, Arthur W Barnard, Joe Finney, Kenji Watanabe, Takashi Taniguchi, MA Kastner, and David Goldhaber-Gordon, “Emergent ferromagnetism near three-quarters filling in twisted bilayer graphene,” *arXiv preprint arXiv:1901.03520* (2019).

[48] M Serlin, CL Tschirhart, H Polshyn, Y Zhang, J Zhu, K Watanabe, T Taniguchi, L Balents, and AF Young, “Intrinsic quantized anomalous hall effect in a moiré heterostructure,” *arXiv preprint arXiv:1907.00261* (2019).

[49] Jiang-Xiazi Lin, Ya-Hui Zhang, Erin Morissette, Zhi Wang, Song Liu, Daniel Rhodes, K Watanabe, T Taniguchi, James Hone, and JIA Li, “Spin-orbit-driven ferromagnetism at half moiré filling in magic-angle twisted bilayer graphene,” *Science* **375**, 437–441 (2022).

[50] Zhiyu Dong, Margarita Davydova, Olumakinde Ogunnaike, and Leonid Levitov, “Isospin- and momentum-polarized orders in bilayer graphene,” *Phys. Rev. B* **107**, 075108 (2023).

[51] Jeil Jung, Marco Polini, and Allan H MacDonald, “Persistent current states in bilayer graphene,” *Physical Review B* **91**, 155423 (2015).

[52] Chunli Huang, Tobias MR Wolf, Wei Qin, Nemin Wei, Igor V Blinov, and Allan H MacDonald, “Spin and orbital metallic magnetism in rhombohedral trilayer graphene,” *Physical Review B* **107**, L121405 (2023).

[53] Ipsita Mandal and Rafael M Fernandes, “Valley-polarized nematic order in twisted moiré systems: In-plane orbital magnetism and crossover from non-fermi liquid to fermi liquid,” *Physical Review B* **107**, 125142 (2023).

[54] Daniel F Agterberg, JC Séamus Davis, Stephen D Edkins, Eduardo Fradkin, Dale J Van Harlingen, Steven A Kivelson, Patrick A Lee, Leo Radzihovsky, John M Tranquada, and Yuxuan Wang, “The physics of pair-density waves: cuprate superconductors and beyond,” *Annual Review of Condensed Matter Physics* **11**, 231–270 (2020).

[55] Tixuan Tan and Trithep Devakul, “Parent berry curvature and the ideal anomalous hall crystal,” *Physical Review X* **14**, 041040 (2024).

[56] Junkai Dong, Taige Wang, Tianle Wang, Tomohiro Soejima, Michael P Zaletel, Ashvin Vishwanath, and Daniel E Parker, “Anomalous hall crystals in rhombohedral multilayer graphene. i. interaction-driven chern bands and fractional quantum hall states at zero magnetic field,” *Physical Review Letters* **133**, 206503 (2024).

[57] Tomohiro Soejima, Junkai Dong, Taige Wang, Tianle Wang, Michael P Zaletel, Ashvin Vishwanath, and Daniel E Parker, “Anomalous hall crystals in rhombohedral multilayer graphene. ii. general mechanism and a minimal model,” *Physical Review B* **110**, 205124 (2024).

[58] Zhihuan Dong, Adarsh S. Patri, and T. Senthil, “Stability of anomalous hall crystals in multilayer rhombohedral graphene,” *Phys. Rev. B* **110**, 205130 (2024).

[59] Adarsh S. Patri, Zhihuan Dong, and T. Senthil, “Extended quantum anomalous hall effect in moiré structures: Phase transitions and transport,” *Phys. Rev. B* **110**, 245115 (2024).

[60] Zhihuan Dong, Adarsh S. Patri, and T. Senthil, “Theory of quantum anomalous hall phases in pentalayer rhombohedral graphene moiré structures,” *Phys. Rev. Lett.* **133**, 206502 (2024).

[61] Michael Sammon, Xiaojun Fu, Yi Huang, Michael A Zudov, Boris I Shklovskii, Geoff C Gardner, John D Watson, Michael J Manfra, Kirk W Baldwin, Loren N Pfeiffer, *et al.*, “Resistivity anisotropy of quantum hall stripe phases,” *Physical Review B* **100**, 241303 (2019).

[62] Tonghang Han, Zhengguang Lu, Yuxuan Yao, Jixiang Yang, Junseok Seo, Chiho Yoon, Kenji Watanabe, Takashi Taniguchi, Liang Fu, Fan Zhang, *et al.*, “Large quantum anomalous hall effect in spin-orbit proximitized rhombohedral graphene,” *Science* **384**, 647–651 (2024).

[63] Yating Sha, Jian Zheng, Kai Liu, Hong Du, Kenji Watanabe, Takashi Taniguchi, Jinfeng Jia, Zhiwen Shi, Ruidan Zhong, and Guorui Chen, “Observation of a chern insulator in crystalline abca-tetralayer graphene with spin-orbit coupling,” *Science* **384**, 414–419 (2024).

METHODS

In this section, we provide detailed discussions to further substantiate the results presented in the main text. Our focus is on the direct connection between time-reversal and rotational symmetry breaking, supported by a comprehensive characterization of magnetic-hysteresis measurement across the low-temperature phase space. Additionally, we elaborate on the extraction of intrinsic anisotropy from the conductivity matrix and discuss the subtleties of interpreting angle-resolved transport data in the presence of stripe order, particularly under conditions of extreme anisotropy.

I. Angle-resolved transport measurement in the linear response regime

To perform angle-resolved transport measurements using a sunflower sample geometry, two configurations— R_{\parallel} and R_{\perp} —are commonly employed, as illustrated in Fig. M1 [26–30]. In the presence of moderate anisotropy, both the longitudinal (R_{\parallel}) and transverse (R_{\perp}) resistances exhibit two-fold angular oscillations as a function of the angle ϕ , described by:

$$R_{\parallel}(\phi) = R_0 - \Delta R \cos 2(\phi - \alpha), \quad (\text{M1})$$

$$R_{\perp}(\phi) = R_H + \Delta R \sin 2(\phi - \alpha), \quad (\text{M2})$$

where ΔR is the oscillation amplitude, R_0 is the mean value of R_{\parallel} , R_H is the average of R_{\perp} , and α denotes the principal axis direction corresponding to the maximum conductivity. According to theoretical analysis [26], Eqs. (M1) and (M2) fully define the linear-response conductivity matrix. The ratio $\Delta R/R_0$, equivalent to the anisotropy parameter ξ in Fig. 2b, provides a quantitative measure of anisotropy strength. A non-zero R_H reflects antisymmetric off-diagonal elements in the conductivity matrix, corresponding to an anomalous Hall effect arising from orbital ferromagnetism [29].

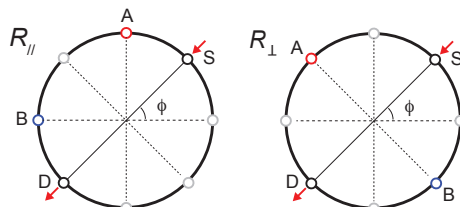


FIG. M1. Angle-resolved transport measurement with the “sunflower” sample geometry. Schematic of the angle-resolved transport measurement setup used to extract R_{\parallel} (left) and R_{\perp} (right) in a sample shaped into the so-called “sunflower” geometry.

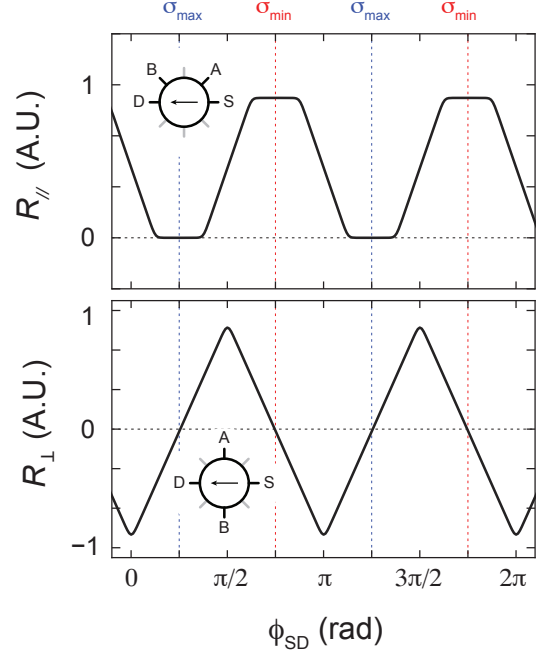


FIG. M2. Expected angular response in the presence of large anisotropy. The angular dependence of R_{\parallel} (top) and R_{\perp} (bottom) corresponding to an intrinsic conductivity anisotropy of $\sigma_{\max}/\sigma_{\min} = 10$.

However, in the presence of extreme transport anisotropy, the angular response is expected to include higher harmonic terms, deviating from the simple two-fold sinusoidal oscillation, as described by Eqs. M1 and M2. The expected angular response, derived following the theoretical framework presented in Ref. [26], is shown in Fig. M2. Here, the principal axes of the anisotropy are aligned along $\phi = 45^\circ$ and 135° . Notably, R_{\parallel} exhibits a prominent plateau around the principal axes. Consequently, R_{\parallel} remains vanishingly small even when the current direction is detuned from the principal axis of maximum conductivity by as much as $\delta\phi \approx 20^\circ$. The presence of this plateau explains the observation of superconducting transport even when the current flow is slightly misaligned from the stripe orientation.

II. Intrinsic anisotropy in the underlying conductivity matrix

Previous theoretical and experimental studies have established a robust framework for extracting the full conductivity matrix from angle-resolved transport measurements [26, 27]. In regimes of moderate anisotropy, the resistance ratio R_{\max}/R_{\min} —determined from R_{\parallel} with current applied along two principal axes—closely approximates the intrinsic conductivity ratio $\sigma_{\max}/\sigma_{\min}$. In this scenario, an anisotropy parameter can be de-

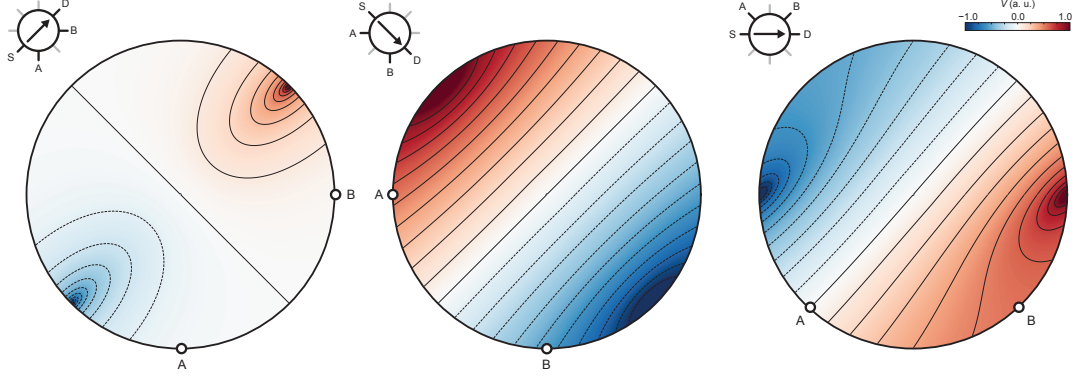


FIG. M3. Potential distribution across a disk-shaped sample in the presence of extreme anisotropy. Simulated potential distribution across a disk-shaped sample with different source and drain configurations, assuming an intrinsic conductivity anisotropy of $\sigma_{\max}/\sigma_{\min} = 5$, where σ_{\max} and σ_{\min} represent the conductivities along the two principal axes of the underlying electronic order. This potential distribution enables the extraction of R_{\parallel} from angle-resolved transport measurements. For current applied along $\phi = 225^\circ$ (left) and $\phi = 135^\circ$ (right), the calculated resistance ratio is $R_{\max}/R_{\min} = 16.5$.

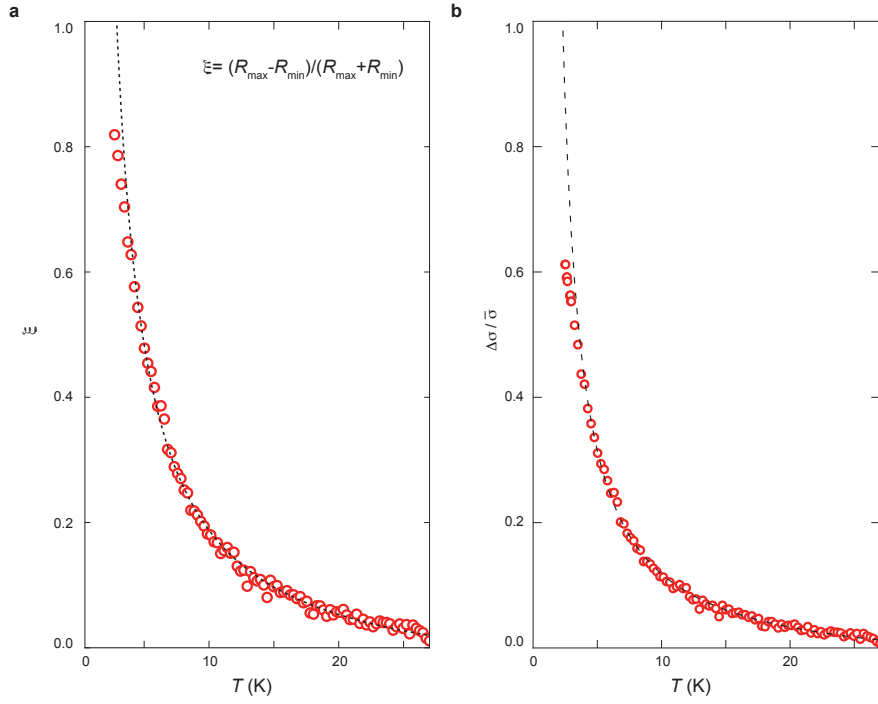


FIG. M4. Anisotropy of resistance and conductance. (a) Temperature dependence of ξ , as defined in Eq. 1. This is the same as Fig. 2a. (b) Temperature dependence of $\Delta\sigma/\bar{\sigma}$. σ_{\max} and σ_{\min} are the intrinsic conductivity along orthogonal principal axes, extracted from the angular dependence of transport response.

defined as $\Delta\sigma/\bar{\sigma}$, where $\bar{\sigma} = (\sigma_{\max} + \sigma_{\min})/2$ and $\Delta\sigma = (\sigma_{\max} - \sigma_{\min})/2$, is largely equivalent to ξ . However, under conditions of extreme anisotropy, this equivalence breaks down: R_{\max}/R_{\min} becomes significantly influenced by the non-uniform potential distribution across the sample, leading to deviations from the true conductivity ratio.

A theoretical framework introduced in Ref. [26] allows us to quantitatively identify the intrinsic anisotropy in

the conductivity matrix based on resistance measurement across the disk-shaped sample. As an illustration, Fig. M3 shows calculated potential distributions across the sample disk for different source-drain configurations, assuming an intrinsic conductivity anisotropy of $\sigma_{\max}/\sigma_{\min} = 5$. When current flows along the axis of maximum conductivity, the potential tends to fan out in the transverse direction due to the anisotropic conductivity tensor. This causes voltage probes aligned with

the current path to underestimate the true voltage drop, leading to an inflated value of the measured resistance ratio. In this example, the resulting resistance anisotropy is $R_{\max}/R_{\min} = 16.5$, more than three times larger than the actual conductivity ratio.

The framework of Ref. [26] offers a method to account for the geometric impact. This allows us to extract $\sigma_{\max}/\sigma_{\min}$ based on R_{\max}/R_{\min} . Fig. M4a plots the temperature dependence of R_{\max}/R_{\min} , which is the same as Fig. 2a. In contrast, Figure M4b presents the temperature evolution of the conductivity ratio $\sigma_{\max}/\sigma_{\min}$. While the ratio of conductivity is suppressed compared to the ratio of measured resistance, we note that the Curie-Weiss behavior remains the same.

Near the nematic transition at $T = 1.5$ K, $\sigma_{\max}/\sigma_{\min}$ exhibits a sharp cusp, with $\sigma_{\max}/\sigma_{\min} \approx 8$ (Fig. 2a inset). This level of anisotropy is comparable to that found in quantum Hall stripe phases, which typically exhibit intrinsic anisotropy ratios in the range of 20–40 [61]. Below 1 K, the ratio $\sigma_{\max}/\sigma_{\min}$ diverges due to the onset of superconductivity. Because the superconducting and stripe orders emerge nearly simultaneously, disentangling their respective contributions to the low-temperature anisotropy remains a significant challenge.

III. Connection between anomalous Hall effect and transport anisotropy

A recent study on rhombohedral hexalayer graphene reports that the emergence of the anomalous Hall effect is directly linked to a nematic transition [29]. Here, we show that a similar correlation arises around the stripe order regime, where the anomalous Hall effect occurs within regions of the n – D phase space characterized by extreme transport anisotropy.

Figure M5a displays a color map of the transport anisotropy, defined as $\xi = (R_{\max} - R_{\min})/(R_{\max} + R_{\min})$, plotted as a function of carrier density n and displacement field D . Regions of strong anisotropy, highlighted in red, appear prominently in the high- D regime surrounding the $SC\ i$ and $SC\ ii$ phases.

Figures M5b–j present magnetic hysteresis loops measured at various n and D values, revealing a clear correlation between the anomalous Hall effect and anisotropic transport. At locations marked by open blue circles in Fig. M5a, the transport response exhibits pronounced magnetic hysteresis (Figs. M5b–d), coinciding with strong anisotropy. In contrast, at the points marked by open red diamonds, angle-resolved measurements reveal suppressed anisotropy and an absence of anomalous Hall response (Figs. M5e–g).

IV. $SC\ i$ and $SC\ ii$ regimes

The emergence of stripe order is a universal feature across the entire parameter space of the $SC\ i$ phase. When current flows perpendicular to the stripes, a highly resistive transport response is observed (middle panel of Fig. M7), signaling the apparent absence of superconductivity in this configuration. This behavior stands in stark contrast to the vanishing R_{\parallel} observed when current is applied parallel to the stripe orientation (left middle panel of Fig. M7). The anisotropic nature of the $SC\ i$ phase is further highlighted by line cuts taken at fixed displacement field D (top panels of Fig. M8).

Even when current is applied transverse to the stripe direction, R_{\perp} drops to zero within the $SC\ i$ region (right panel of Fig. M7, bottom panels of Fig. M8). This observation is consistent with superconductivity developing exclusively along the stripes, which equalizes the potential along their direction, thus resulting in a vanishing R_{\perp} despite a finite, resistive R_{\parallel} . Moreover, the extreme anisotropy appears to be unique to the $SC\ i$ phase. Fig. M9 shows the transport response measured along a diagonal line crossing both the $SC\ i$ and $SC\ ii$ phases. While R_{\parallel} exhibits a pronounced discrepancy between the directions parallel and perpendicular to the stripe order in $SC\ i$, this discrepancy vanishes in $SC\ ii$.

In the n – D region surrounding the $SC\ i$ phase, the principal axis aligns with $\phi = 135^\circ$ (see Fig. 1d). Therefore, a non-zero R_{\perp} measured along $\phi = 135^\circ$ indicates a finite anomalous Hall coefficient in this regime. The right panel of Fig. M7 shows R_{\perp} , revealing that both the $SC\ i$ phase is embedded within a broader region exhibiting a robust anomalous Hall effect.

V. Insulating and superconducting responses

Within the $SC\ i$ phase, both insulating and superconducting behaviors are observed, depending on the measurement configuration. These responses reflect the strong transport anisotropy imposed by the stripe charge order.

Insulating Behavior. Insulating transport is observed in the following configurations:

- When current flows perpendicular to the stripe orientation, R_{\parallel} shows insulating behavior at low temperatures (Fig. M10a, c, d).
- When current flows at an angle to the stripe orientation—such as $\phi = 270^\circ$ —the voltage response measured perpendicular to the stripes exhibits insulating behavior (Fig. M10a).

Superconducting Behavior. Superconducting transport, characterized by vanishing resistance, is observed under the following conditions:

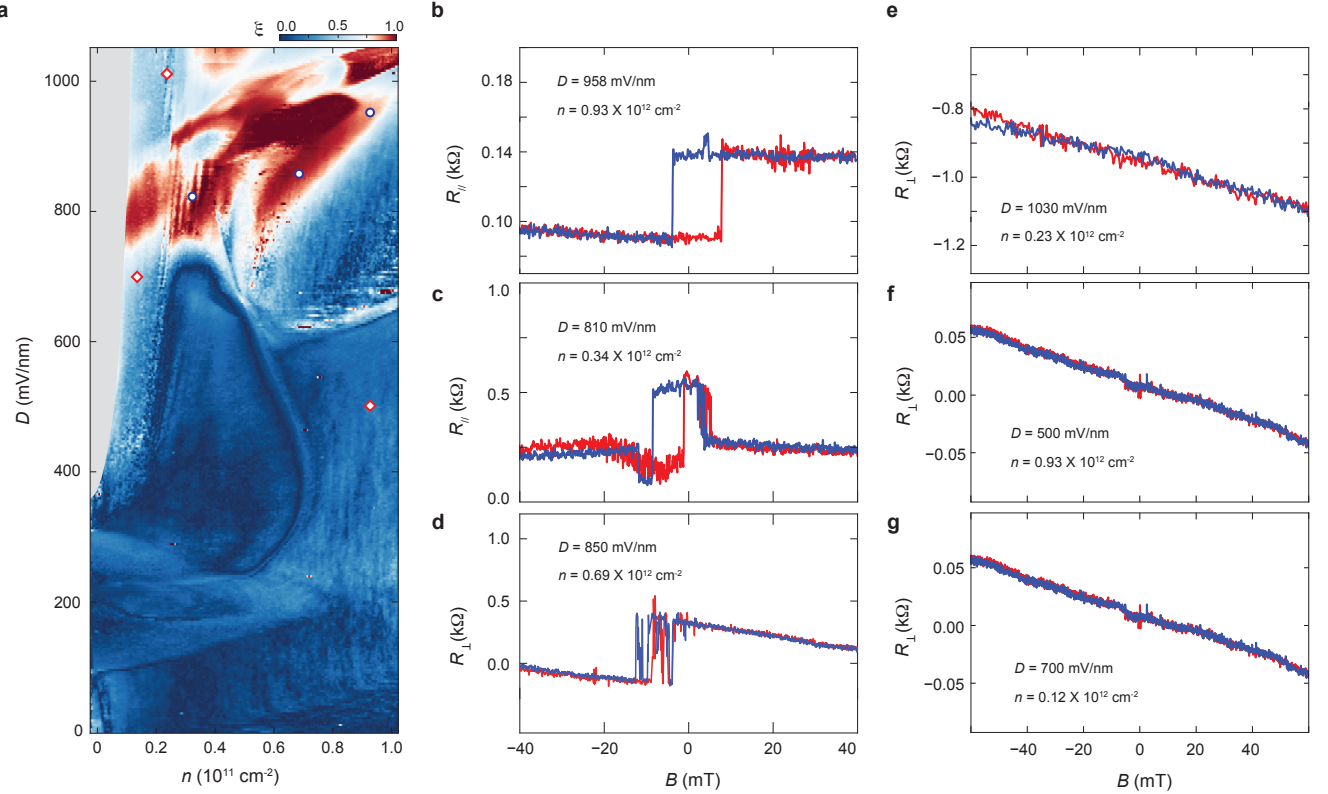


FIG. M5. **Evolution of transport anisotropy across the low-temperature phase diagram.** (a) Color map of ξ , defined as Eq. 1, plotted as a function of carrier density n and displacement field D . Regions of extreme anisotropy are shown in red on the chosen color scale, while blue and dark blue indicate more isotropic transport responses. (b–g) Transport responses measured at different n and D values as an out-of-plane magnetic field is swept back and forth. Magnetic hysteresis loops, indicative of orbital ferromagnetism, are observed in regimes exhibiting strong transport anisotropy, marked by blue open circles. By contrast, regions with weaker anisotropy in panel (a), marked by red open diamonds, show no magnetic hysteresis as demonstrated in panels (e–g).

- When current flows parallel to the stripe orientation, R_{\parallel} shows superconducting behavior at low temperatures (Fig. M11a).
- When current flows at an angle to the stripe orientation, such as $\phi = 270^\circ$, the voltage response measured parallel to the stripe direction exhibits superconducting behavior (Fig. M11c).
- Under the same angled configuration ($\phi = 270^\circ$), R_{\parallel} also shows superconducting behavior, although with a reduced T_c (Fig. M11b).

These observations underscore the intrinsic one-dimensional nature of superconductivity in the $SC\ i$ phase and the critical role of stripe orientation in defining transport response.

The observation of superconducting behavior in R_{\parallel} along $\phi = 270^\circ$ is particularly noteworthy. In this configuration, the voltage response is measured across multiple stripes, as illustrated in the inset of Fig. M11b. The vanishing R_{\parallel} in this scenario could originate from two possible mechanisms: (i) adjacent stripes are coherently cou-

pled via Josephson tunneling, enabling phase coherence across stripes and resulting in zero resistance when measured perpendicular to their orientation; (ii) the stripe pattern forms local domains that happen to connect contacts A and B in this particular geometry, enabling superconducting paths along irregular orientations.

Both interpretations reflect the complex spatial structure of superconductivity in the $SC\ i$ phase and highlight the role of stripe domain configuration in determining transport behavior.

Notably, measurements performed perpendicular to the stripe orientation consistently exhibit a distinctive low-temperature cusp in resistance (Fig. M10). A plausible origin of this resistance cusp is the onset of stripe charge order. The highest superconducting transition temperature (T_c)—measured with current flowing parallel to the stripes—emerges consistently just below stripe formation. This observation strongly suggests that superconductivity develops directly from the pre-existing stripe-ordered state.

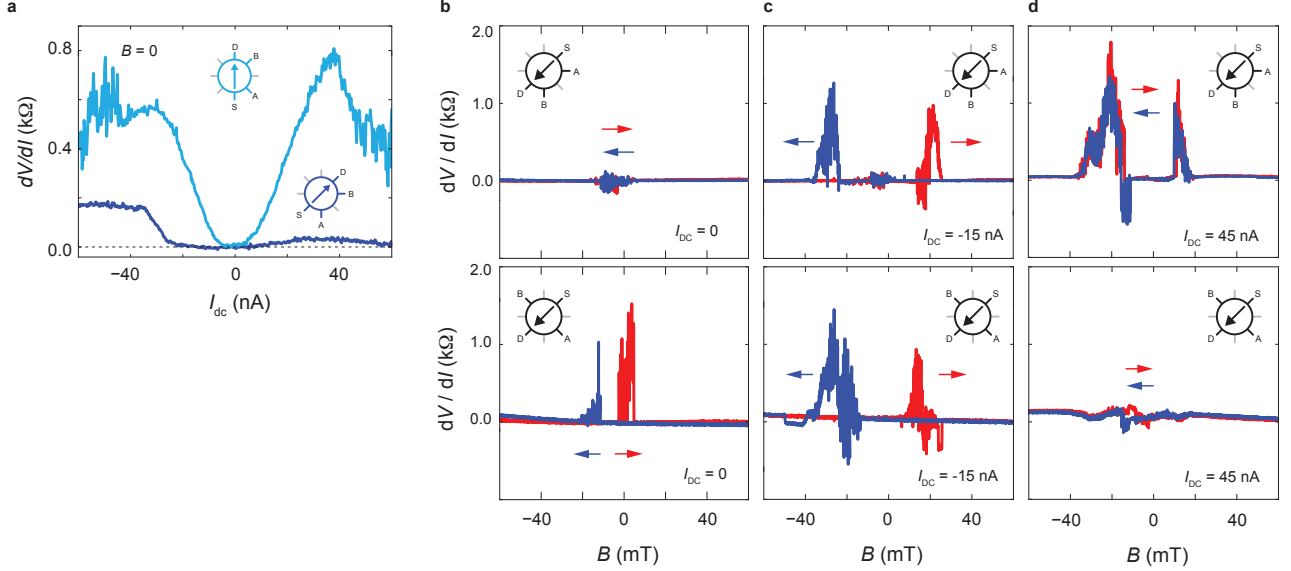


FIG. M6. B_{\perp} -driven hysteresis transitions with a d.c. current bias. (a) I-V characteristic of the $SC\ i$ phase measured with different current flow direction. When current is applied along the stripe orientation, critical supercurrent I_c , defined by the onset in differential resistance dV/dI , is roughly 20 nA. (b-d) B_{\perp} -induced hysteresis measured with a d.c. current bias of (b) $I_{dc} = 0$, (c) 15 nA, and 45 nA. In panel (b-d), current bias is applied along the stripe orientation. Top and bottom panel plot dV/dI measured parallel and transverse to the current flow direction, respectively.

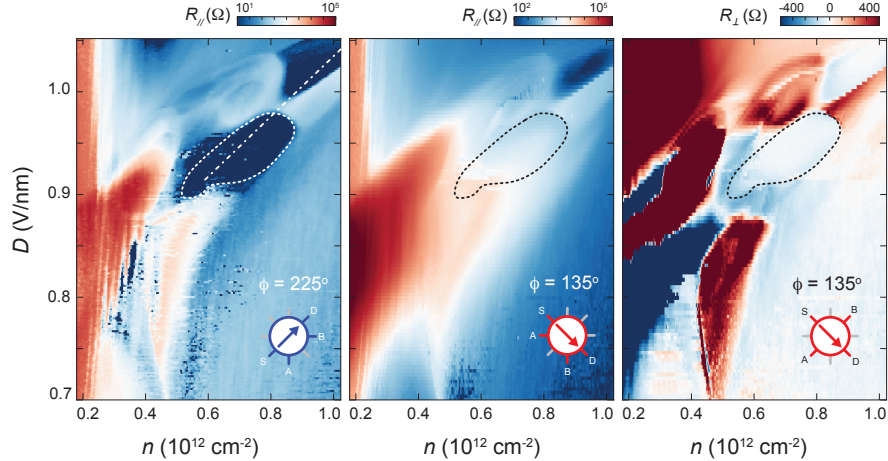


FIG. M7. $SC\ i$ and $SC\ ii$ regimes. Color map of R_{\parallel} at $\phi = 225^\circ$ (left, along the stripe orientation), R_{\parallel} at $\phi = 135^\circ$ (middle, perpendicular to the stripe orientation), and R_{\perp} at $\phi = 135^\circ$ (right, perpendicular to the stripe orientation), measured as a function of n and D around the $SC\ i$ and $SC\ ii$ regimes.

VI. Angular interplay between superconducting and metallic phases

Recent work has shown that superconductivity in magic-angle twisted trilayer graphene exhibits a distinctive angular interplay with the metallic phase above the superconducting transition [30]. Specifically, the most robust superconducting response—characterized by the highest critical current and transition temperature—emerges along the direction of maximum resistivity

(i.e., minimum conductivity) in the metallic state.

In contrast, the $SC\ i$ phase displays the opposite angular correlation. Due to the emergence of stripe order, superconducting transport is confined along the direction of maximum conductivity in the metallic state above the superconducting transition temperature. Interestingly, although $SC\ ii$ does not exhibit clear signatures of stripe order, they follow the same angular correlation as $SC\ i$ —with superconductivity preferentially developing along the direction of highest conductivity in the normal

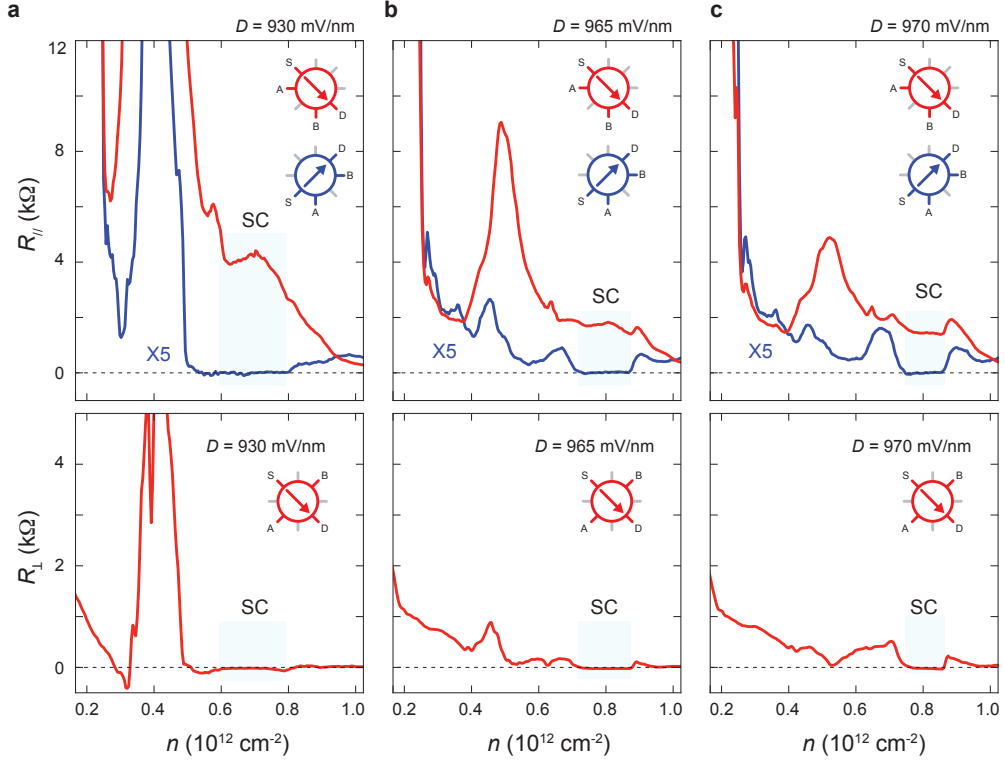


FIG. M8. **Density line cuts across the *SC i* phase.** Line cuts taken at fixed displacement fields from the n – D maps in Fig. M7, shown for (a) $D = 0.93$ V/nm, (c) $D = 0.965$ V/nm, and (d) $D = 0.97$ V/nm. The top panels show R_{\parallel} , and the bottom panels show R_{\perp} . The blue trace is multiplied by a factor of 5 for clarity.

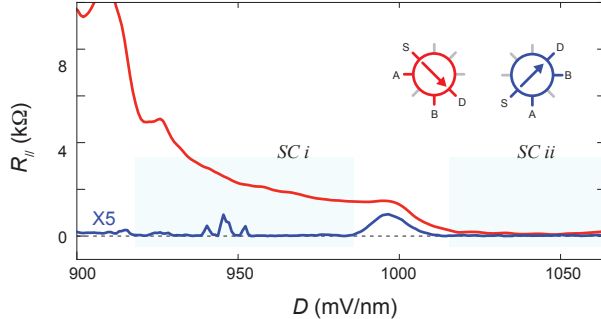


FIG. M9. **Across *SC i* and *SC ii* regimes.** Longitudinal resistance R_{\parallel} measured along the diagonal dashed line shown in Fig. M7a, traversing both superconducting pockets *SC i* and *SC ii*.

state.

Figure M13 examines the angular interplay of a superconducting phase emerging from the low- D regime of the R6G sample. Following the method established in Ref. [30], we compare the angular dependence of the critical supercurrent I_c —defined by the position of maximum dV/dI in the I-V characteristics—with the transport anisotropy of the metallic phase. Anisotropy in the metallic state is characterized by the angular dependence of R_{\parallel} and R_{\perp} . Fitting the data using Eqs. M1–M2 reveals two principal axes: the direction of minimum resistivity (maximum conductivity), marked by the vertical green

dashed line, and the direction of maximum resistivity, marked by the gray dashed line. As shown in Fig. M13e, the maximum I_c aligns with the direction of maximum conductivity, while the minimum I_c occurs along the direction of minimum conductivity.

According to theoretical arguments based on a simple Ginzburg–Landau framework, this angular behavior is consistent with a uniform superconducting gap and an anisotropic effective mass. Notably, this rules out order parameter structures involving a mixture of *s*- and *d*-wave components but remains consistent with a pure *s*-wave symmetry or certain *p*-wave states [30].

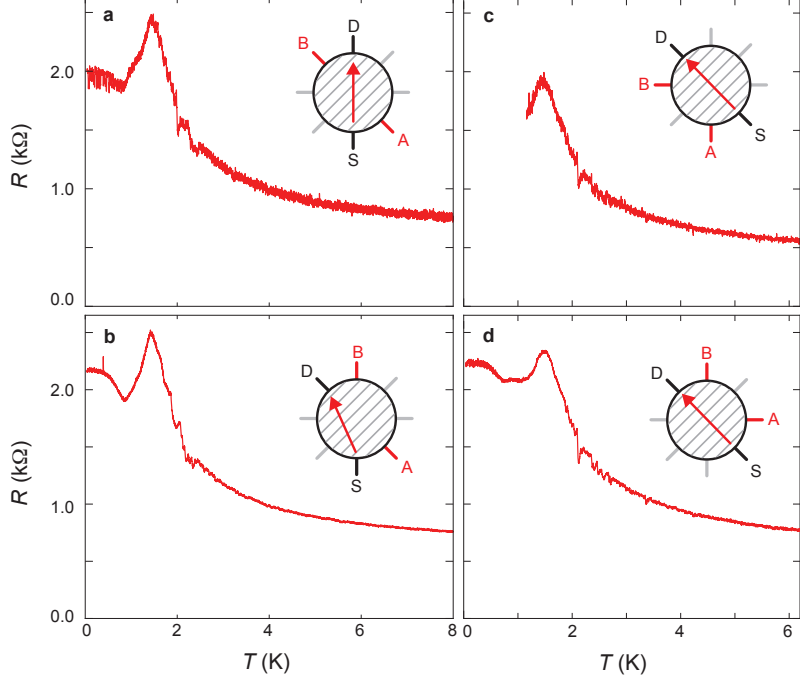


FIG. M10. **Configurations with insulating behaviors.** Insulating response is observed between contacts aligned perpendicular to the stripe orientation. Current does not need to flow perpendicular to the stripes to generate the insulating behavior, as demonstrated by panel (a) and (b).

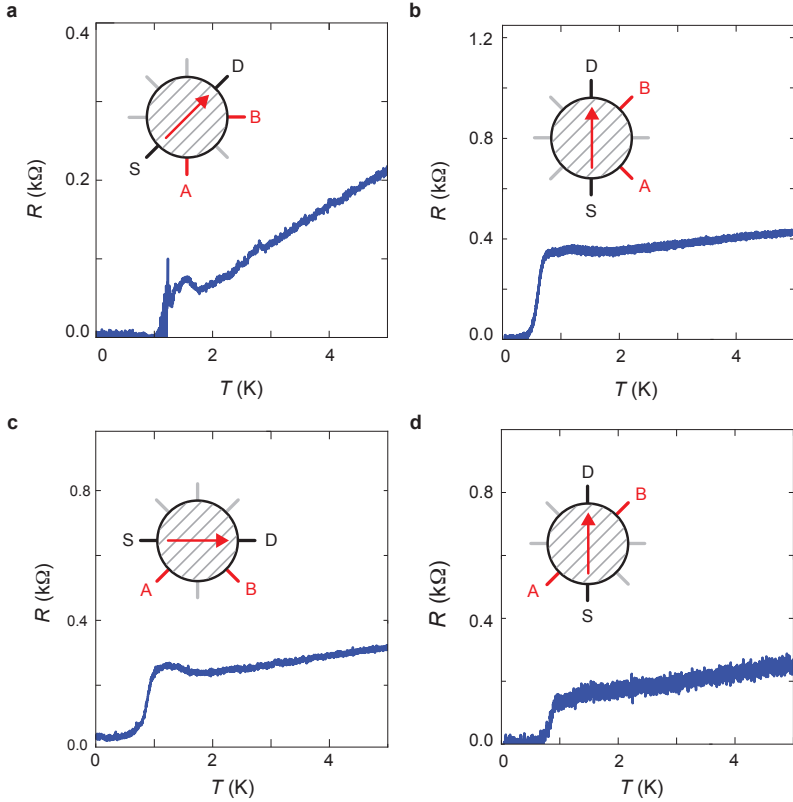


FIG. M11. **Configurations with superconducting behaviors.** The superconducting transition temperature, defined by the temperature where resistance vanishes to zero, is highly dependent on the direction of current flow, as well as the direction of measurement.

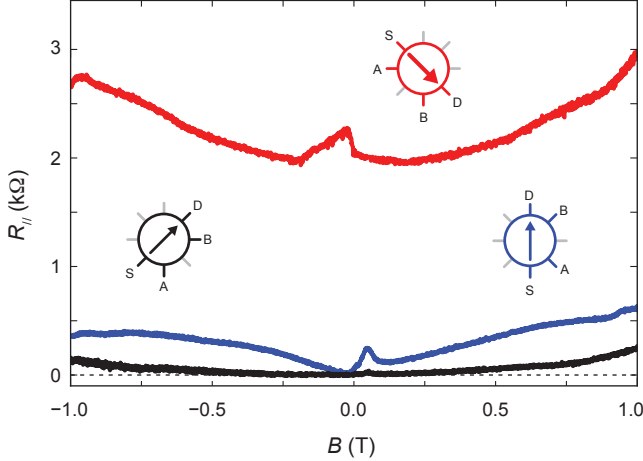


FIG. M12. **Dependence on B_{\perp} .** R_{\parallel} as a function of B_{\perp} measured with current being applied along different directions.

VII. Rhombohedral hexalayer graphene

Figure M14 determines the layer number of the rhombohedral sample by extracting the Chern number of a valley-polarized state that emerges near charge neutrality, close to the layer-polarization transition (Fig. M14a). Previous studies have established that the Chern number of this state is directly correlated with the number of layers in rhombohedral graphene [62, 63]. The extracted Chern number, together with the observed transport responses, confirms that the sample is rhombohedral hexalayer graphene.

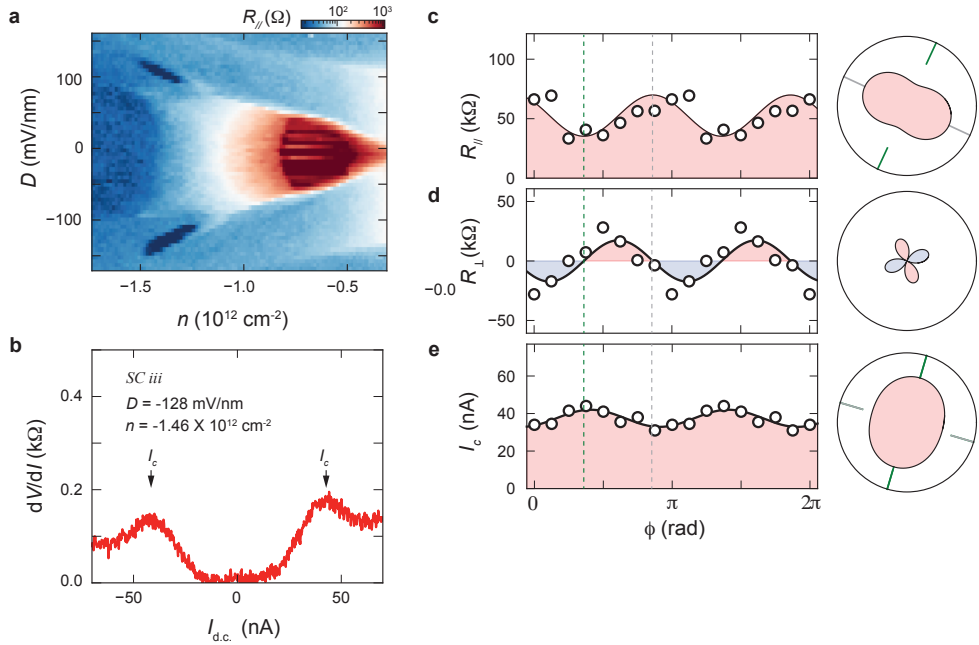


FIG. M13. **The angular dependence of SC iii.** (a) $n - D$ map of R_{\parallel} around the superconducting phase in the low- D regime. (b) I-V characteristics measured from the low- D SC phase. Critical current I_c is defined by the peak position in the differential resistance dV/dI . (c-d) Angular dependence of R_{\parallel} and R_{\perp} measured from the normal state at $T = 1.5 \text{ K}$ and the same n and D as panel (b). Black solid line is the best fit to data using Eq. M1-2. (e) Angular dependence of I_c . Green vertical dashed line mark the direction of maximum conductivity (minimum resistivity) in the normal state, which corresponds to the direction of maximum I_c in the superconducting phase.

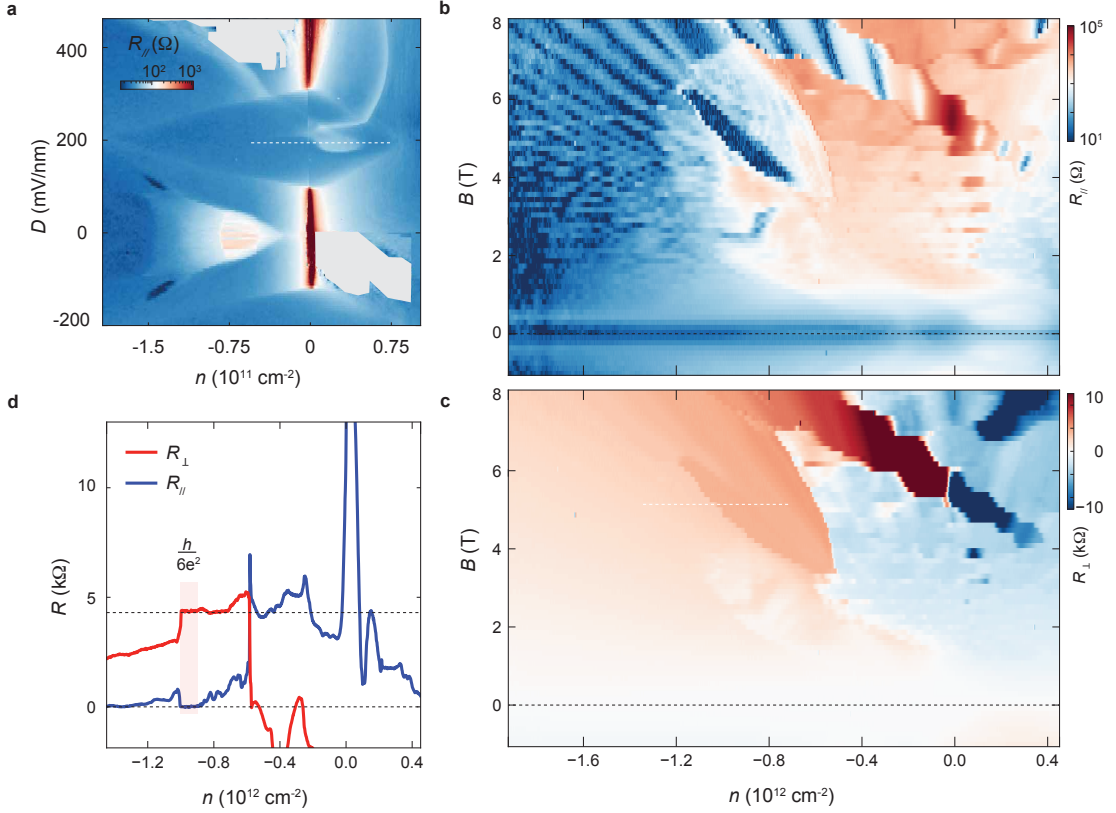


FIG. M14. **Identification of rhombohedral hexalayer.** (a) Color scale map of R_{\parallel} measured as a function of n and D . The white dashed line cuts across the anomalous Hall effect regime near $D = 200 \text{ mV/nm}$. Color scale map of (b) R_{\parallel} and (c) R_{\perp} as a function of n and B , taken at the D value corresponding to the white dashed line in panel (a). (c) R_{\parallel} and R_{\perp} as a function of n , measured along the white dashed line in panel (c). The observed plateau in R_{\perp} coinciding with vanishing R_{\parallel} , points to rhombohedral stacking hexalayer graphene.

SUPPLEMENTARY MATERIALS

Superconductivity, Anomalous Hall Effect, and Stripe Order in Rhombohedral Hexalayer Graphene

Erin Morissette*, Peiyu Qin*, Hai-Tian Wu, Naiyuan James Zhang, Kenji Watanabe, Takashi Taniguchi, and J.I.A. Li[†]

[†] Corresponding author. Email: jia.li @brown.edu

I. The impact of angular sequence on magnetic hysteresis loops

A sequential measurement that rotates through different current flow directions has a striking effect on first-order transitions. Here, we investigate the impact of such a protocol on the magnetic hysteresis transition, using the same rhombohedral hexalayer graphene sample. Figure S1a shows the magnetic hysteresis loop obtained using a fixed measurement configuration, as the out-of-plane magnetic field is swept back and forth. The observed hysteresis arises from the formation of magnetic domains and the finite energy barrier associated with domain wall motion.

In contrast, Fig. S1b shows the Hall coefficient measured using a sequential scheme, where the current direction is rotated through multiple angles at each magnetic field value. Remarkably, this angular rotation suppresses the magnetic hysteresis, effectively collapsing the forward and reverse B -sweep curves onto a single trajectory.

These results suggest that angularly sequential measurements significantly influence magnetic domain wall dynamics, possibly by preventing domain wall pinning or facilitating relaxation toward the equilibrium ground state. Consequently, this measurement approach provides a powerful tool for probing equilibrium behavior across first-order magnetic transitions.

This finding also sheds new light on the sequential measurements shown in Fig. S2c, where a similar protocol leads to a marked suppression of the superconducting transition temperature. The results raise the possibility that angular current rotation dramatically alters the domain structure of the stripe order, thereby strongly impacting the superconducting transition.

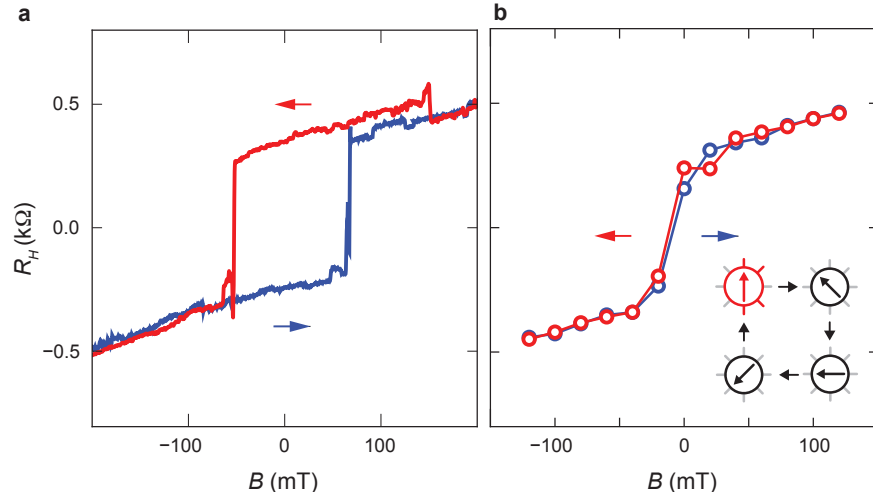


FIG. S1. The impact of angular sequence on first order transitions. (a) R_H measured at fixed n and D in the multiferroic state, as an out-of-plane magnetic field B is swept back and forth, showing clear magnetic hysteresis. (b) Sequential measurement performed at the same n and D values as in panel (a), where all current directions are cycled through before B is ramped to the next value. The angular sequence suppresses the hysteresis, collapsing the forward and reverse B sweeps onto a single curve.

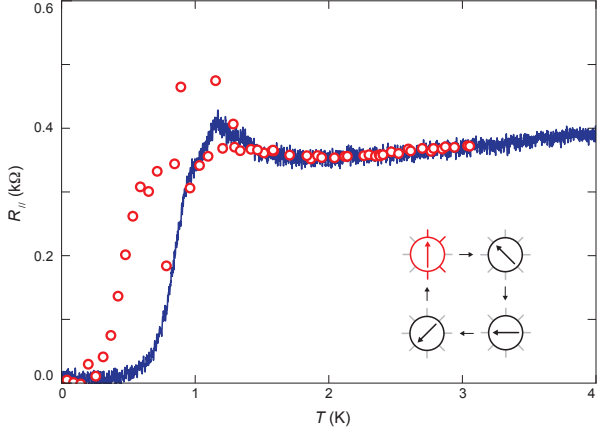


FIG. S2. Angular control of the superconducting transition. R - T curves of the $SC\ i$ phase measured on warming. Open red circles represent data obtained using a sequential angular protocol: R_{\parallel} is measured with an a.c. current of 4nA applied along $\phi = 270^\circ$, while between consecutive measurements, current is sequentially rotated through $\phi = 135^\circ$, 180° , and 225° (illustrated in the bottom-right inset). The dark blue trace corresponds to continuous measurements without configuration switching and is identical to the reference curve shown in Fig. S3a. While configuration switching has negligible impact at higher temperatures, it induces significant hysteretic variations in the transport response near the superconducting transition.

II. The impact of angular sequence on superconducting transitions

The most pronounced variation in T_c is induced by a specific measurement sequence, wherein an a.c. current of 3nA is sequentially applied along directions $\phi = 135^\circ$, 180° , 225° , and 270° . During this sequence, the transport response (R_{\parallel}) is measured exclusively at $\phi = 270^\circ$ (red open circles in Fig. 3c) and compared against a reference R - T curve (blue trace), taken from Fig. S3a, which corresponds to continuous measurements performed without changing the current direction.

While the configuration switching has negligible influence at higher temperatures, it induces a marked suppression of the superconducting transition temperature T_c , as well as enhanced variability in R_{\parallel} near $T = 1$ K. These fluctuations reflect abundant switching events in the transport response, suggestive of a dynamic reconfiguration of the underlying electronic order.

Although the impact of sequential measurements has not been extensively explored in prior studies, its pronounced effect here is striking. A plausible explanation is that the sequential current reorients the stripe order—consistent with the strong dependence of T_c on current direction shown in Fig. 2a. This provides further evidence that the superconducting transition is intimately tied to the orientation of the stripe phase.

Further evidence of this tunability emerges in the form of current-driven switching observed in the I-V characteristics. As shown in Fig. S4, the differential resistance dV/dI displays numerous current-induced transitions at low B_{\perp} , appearing as discontinuous jumps or fluctuations in the signal. These features are largely suppressed once B_{\perp} exceeds 0.1 T, highlighting the sensitivity of the superconducting state to both current direction and applied magnetic field.

III. Hysteresis across the superconducting transition on warming

Hysteretic behaviors are observed across the temperature-driven superconducting transition. Figure S3 shows R - T curves from five consecutive measurements, all performed at identical carrier density (n), displacement field (D), and using the same warming rate. While the curves exhibit highly reproducible behavior at elevated temperatures, they bifurcate distinctly below the temperature marked by the vertical dashed line, which corresponds to the resistance cusp associated with the nematic transition. This bifurcation results in clearly separated superconducting transitions.

These variations reveal different forms of hysteresis in the R - T characteristics: (i) changes in the superconducting transition temperature T_c ; and (ii) the appearance or absence of a resistance peak above T_c . While the exact nature of these hysteretic effects remains an open question, they could arise from two possible mechanisms.

First, the hysteresis may originate from the nematic transition itself. Previous angle-resolved measurements in graphene moiré systems [30] have shown that thermal cycling can induce variations in transport anisotropy, which may in turn lead to fluctuations in the superconducting transition temperature.

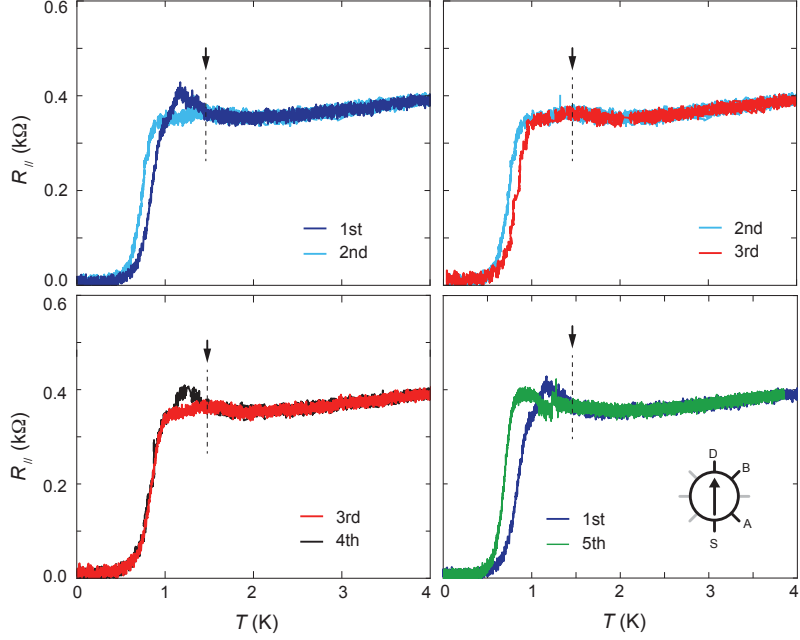


FIG. S3. Hysteresis near the superconducting transition on warming. R - T curves from four consecutive measurements, all performed at identical carrier density (n), displacement field (D), and using the same warming rate. The traces exhibit several distinct forms of hysteresis: shifts in the superconducting transition temperature (T_c), the presence or absence of a resistance peak just above T_c , and discontinuous jumps in the R - T curve (green trace in the bottom right panel).

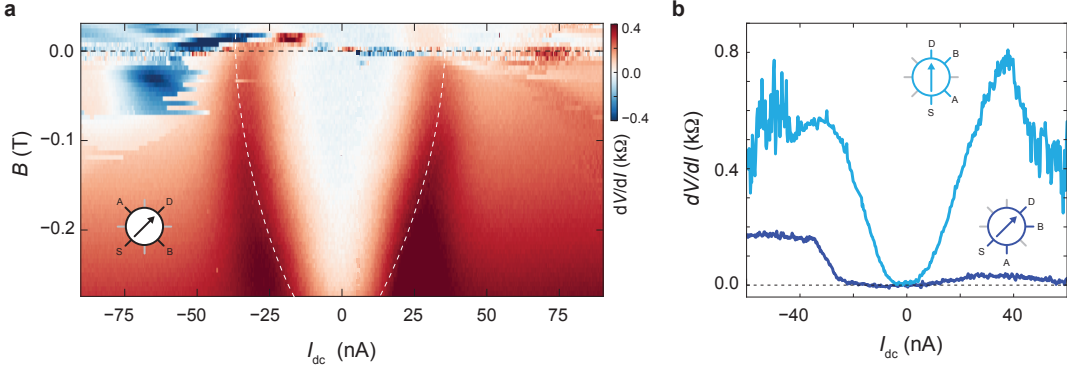


FIG. S4. Current-voltage characteristic of the SC i phase. (a) Color scale map of differential resistance measured as a function of d.c. current bias and out-of-plane magnetic field. The measurement is performed at $n = 0.8 \times 10^{12} \text{ cm}^{-2}$ and $D = 958 \text{ mV/nm}$, with current flowing along the stripe orientation. (b) dV/dI as a function of d.c. current measured at $B = 0$ with different ϕ .

Second, the hysteresis observed during warming could be associated with the formation of stripe order. As demonstrated in Fig. 3, superconductivity and stripe order emerge concurrently. Therefore, the observed variations in the superconducting transport response may arise from subtle changes in the stripe configuration between successive temperature cycles.

IV. Temperature Control During warming and cooling measurements

Controlled warming and cooling measurements shown in Fig. 3 are carried out using a BlueFors dilution refrigerator. Temperature control is implemented through the following procedures: (i) A resistive heater located on the sample probe provides localized heating. (ii) Heater power is regulated via feedback control based on the probe temperature.

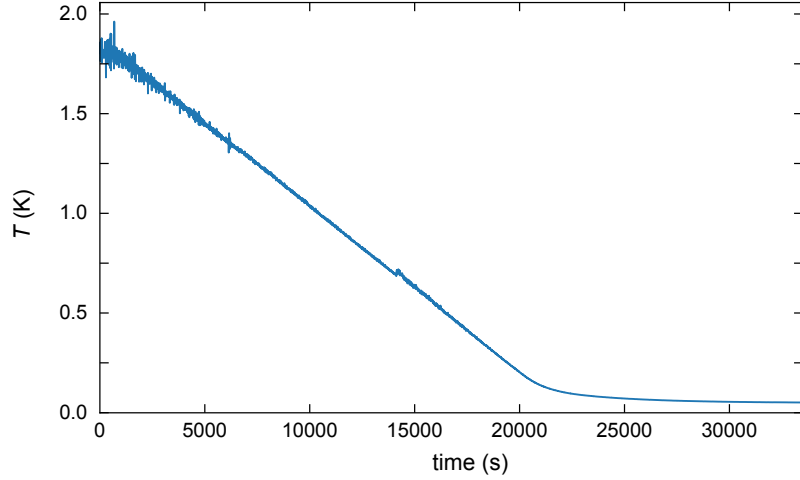


FIG. S5. **Controlled cooling measurement.** Temperature as a function of time during the controlled cooling process shown in Fig. 3. Here, the probe is cooled from 1.6 K to 30 mK over the course of 7 hours.

(iii) The temperature set point is continuously ramped at a predefined rate.

Measurements during warming are performed under standard conditions for quantum transport experiments in two-dimensional materials. Starting from the base temperature, the dilution refrigerator is switched to a safe circulation mode. A controlled temperature ramp is applied via the sample stage heater, with a typical warming rate set between 8 mK/min and 20 mK/min.

Cooling measurements are conducted in two distinct regimes. For temperatures above $T > 1.5$ K, cooling is achieved using the safe circulation mode alone. The desired cooling rate is obtained by balancing the natural cooling from the circulation flow with controlled heating from the heater. For $T < 1.5$ K, cooling is carried out by condensing the $^3\text{He}/^4\text{He}$ mixture and operating the dilution unit. In this regime, the cooling rate is similarly regulated by adjusting the heater power to counterbalance the cooling capacity of the dilution stage.

An example of a controlled cooling cycle is shown in Fig. S5, where the sample temperature T is ramped from 1.6 K to 30 mK at a constant rate of 0.07 mK/min. As illustrated, the temperature evolution closely follows the programmed ramp rate, demonstrating the high degree of control achievable during such cooling measurements.